Journal of Electronic Materials

Improved Photoelectrochemical Performance of Chemically Grown Pristine Hematite Thin Films

--Manuscript Draft--

Manuscript Number:	JEMS-D-21-00919R5
Full Title:	Improved Photoelectrochemical Performance of Chemically Grown Pristine Hematite Thin Films
Article Type:	Original Research
Keywords:	hematite; Photocurrent; hydrogen generation; electrochemical impedance; electron lifetime; AACVD
Corresponding Author:	Safeer Ahmed Quaid-i-Azam University Islamabad, PAKISTAN
Corresponding Author Secondary Information:	
Corresponding Author's Institution:	Quaid-i-Azam University
Corresponding Author's Secondary Institution:	
First Author:	Saima Qureshi
First Author Secondary Information:	
Order of Authors:	Saima Qureshi
	Duncan H. Gregory
	Asif Ali Tahir
	Safeer Ahmed
Order of Authors Secondary Information:	
Funding Information:	Higher Education Commision, Pakistan (IRSIP; No. 1-8/HEC/HD/2017/8222) — Ms. Saima Qureshi
Abstract:	The alpha phase of hematite (α-Fe 2 O 3) is one of the most promising catalysts for photoelectrochemical (PEC) water splitting amongst several photoanode materials due to its suitable bandgap and stability in aqueous solutions. The surface structure and morphology of films play pivotal roles in the enhancement of water oxidation reaction kinetics. In this work, α-Fe 2 O 3 films were produced via either spray pyrolysis (SP), chemical vapor deposition (CVD) or aerosol-assisted chemical vapor deposition (AACVD). Their structural and morphological properties were subsequently characterized by powder X-ray diffraction (PXD), scanning electron microscopy (SEM) and Raman spectroscopy. High quality thin films were best achieved by AACVD annealed at 525 ° C, possessing an average thickness of 0.75μm with 85% transmittance and an optical absorption onset at 650 nm. The results evidently showed that the thermal oxidation process achieved at 525°C eliminated undesired impurity phases such as FeO and Fe 3 O 4 and enabled the microstructure to be optimized to facilitate the generation and transport of photogenerated charge carriers. The optimized α-Fe 2 O 3 film showed a stable PEC water oxidation current density of ~1.23 mA cm -2 at 1.23 V (vs. RHE), with an onset potential of 0.76 V, under AM 1.5 irradiation. The obtained higher current density of pristine α-Fe 2 O 3 thin films obtained by AACVD method is unique and the films presented good photocurrent stability with 92% retention after 6 h. Data form electrochemical impedance spectroscopy (EIS) corroborated these results, identifying fast charge transfer kinetics with decreased resistance and an electron lifetime of 175 μs. Quantitative measurements showed that 1.2 μmol cm -2 of oxygen could be produced at the photoanode in 6 h.

Improved Photoelectrochemical Performance of Chemically Grown Pristine Hematite Thin Films

Saima Qureshi[a,b,] Duncan H. Gregory[b], Asif Ali Tahir [c], Safeer Ahmed[a,] *

Department of Chemistry, Quaid-i-Azam University, 45320, Islamabad, Pakistan.

WestCHEM, School of Chemistry, University of Glasgow, Glasgow G12 8QQ, United Kingdom.

Environment and Sustainability Institute (ESI), University of Exeter, Penryn Campus, TR10 9FE, United Kingdom.

*Corresponding author's e-mail addresses: safeerad@qau.edu.pk

Tel: 00-92-51-90642145, Fax: 00-92-51-90642241

Abstract

The alpha phase of hematite (α-Fe_2O_3) is one of the most promising catalysts for photoelectrochemical (PEC) water splitting amongst several photoanode materials due to its suitable bandgap and stability in aqueous solutions. The surface structure and morphology of films play pivotal roles in the enhancement of water oxidation reaction kinetics. In this work, α-Fe_2O_3 films were produced via either spray pyrolysis (SP), chemical vapor deposition (CVD) or aerosol-assisted chemical vapor deposition (AACVD). Their structural and morphological properties were subsequently characterized by powder X-ray diffraction (PXD), scanning electron microscopy (SEM) and Raman spectroscopy. High quality thin films were best achieved by AACVD annealed at 525°C, possessing an average thickness of 0.75µm with 85% transmittance and an optical absorption onset at 650 nm. The results evidently showed that the thermal oxidation process achieved at 525°C eliminated undesired impurity phases such as FeO and Fe_3O_4 and enabled the microstructure to be optimized to facilitate the generation and transport of photogenerated charge carriers. The optimized α-Fe_2O_3 film showed a stable PEC water oxidation current density of ~1.23 mA cm^{-2} at 1.23 V (vs. RHE), with an onset potential of 0.76 V, under AM 1.5 irradiation. The obtained higher current density of pristine α-Fe_2O_3 thin films obtained by AACVD method is unique and the films presented good photocurrent stability with 92% retention after 6 h. Data form electrochemical impedance spectroscopy (EIS) corroborated these results, identifying fast charge transfer kinetics with decreased resistance and an electron lifetime of 175 µs. Quantitative measurements showed that 1.2 µmol cm^{-2} of oxygen could be produced at the photoanode in 6 h.

Key words: hematite; photocurrent; hydrogen generation; electrochemical impedance; electron lifetime; AACVD.

Graphical Abstract

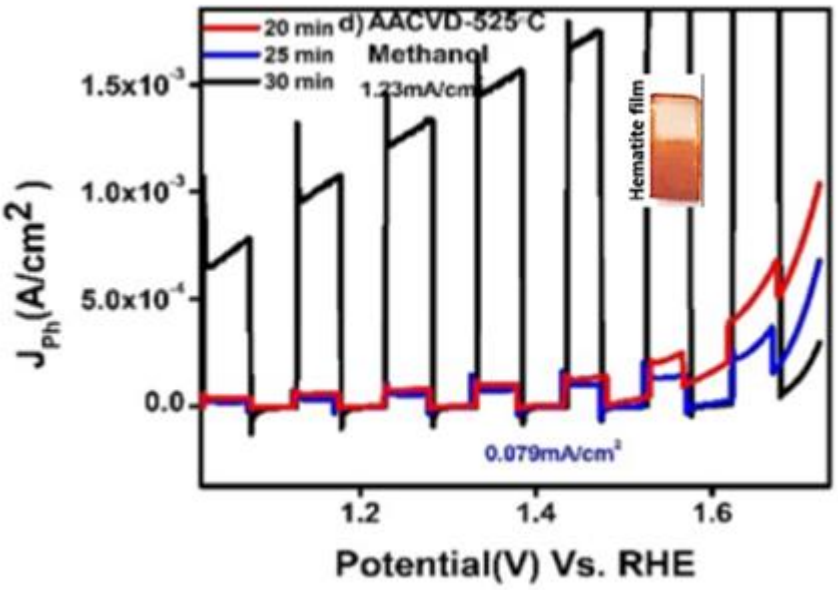

1. Introduction

The photoelectrochemical (PEC) generation of hydrogen is one of the most promising ways to make the best use of renewable solar energy. In a PEC cell, water molecules are broken into hydrogen and oxygen gases on the surfaces of the photocathode and photoanode, respectively. For a material to act as a photocatalyst in a PEC cell, it needs a suitable band gap in the range of 1.23 to 1.6 eV [1]. Further, the valance and conduction band edges should be compatible with the standard electrode potentials of hydrogen gas and oxygen gas evolution. More specifically for the water reduction reaction (H^+/H_2), the conduction band edge of the material needs to be at a potential less than (more negative than) 0 V vs. normal hydrogen electrode (NHE) while the valence band needs to be at a potential higher than (more positive than) 1.23 V vs. NHE for water oxidation (H_2O/O_2). This demands the material must have a light absorption onset at or slightly below 1008 nm [2].

It is well recognized that photocatalysts which utilize ultraviolet (UV) light for hydrogen production via solar water splitting perform better than those which utilize only the visible part of the spectrum due to the higher energy photons

that exist in the former case. On the other hand, the relative proportions of UV (<400 nm), visible (400–800 nm) and infrared (>800 nm) light in the solar spectrum are 4%, 53% and 43%, respectively. Therefore, it is critical to design a photocatalyst which can combine both a high absorption coefficient with a wide absorption window. Consequently, a relatively low-efficiency photocatalyst that is able to absorb a significant portion of visible light can be more useful than a higher-efficiency photocatalyst that absorbs solely in the ultraviolet regime.

Among potentially suitable oxide semiconductor materials such as TiO_2 (with a band gap, E_g, of 3.2 eV), ZnO (E_g = 3.1 eV), and WO_3 (E_g = 2.7 eV), hematite, α-Fe_2O_3 (E_g = 2.1 eV) is considered most promising for PEC water splitting given that it can absorb a major portion of visible light; it possesses excellent stability under alkaline conditions and that it is environmentally benign, earth-abundant (constituting 6.3% of the Earth's crust) and of low cost [3]. The relatively small band gap compared to its oxide competitors, enables it to harvest around 40% of the solar spectrum (up to ~600 nm wavelength). Although, hematite has a theoretical solar-to-hydrogen (STH) efficiency of 14-15%, which is very impressive [4], however, the reported experimental efficiencies for hematite photoanodes are significantly lower. This disparity is mainly due to the short hole diffusion length (2-4 nm) when compared with the single-path optical absorption length or maximum light penetration depth of 118 nm in hematite at a wavelength of 550 nm [4]. Consequently, one can consider only the holes which are produced in the proximity of the hematite/electrolyte interface to participate in water oxidation and generate the photocurrent. Conversely, the holes generated further away from the hematite/electrolyte interface are lost to charge recombination processes. Therefore, the challenge lies in improving the charge carrier diffusion length and maximizing the optical absorption depth while maintaining an appropriate film thickness.

To overcome such limitations, several strategies have been developed to improve the PEC properties of α-Fe_2O_3 such as by modifying the electronic structure via elemental doping [1,3], by synthesizing nanostructured α-Fe_2O_3) [3,4], by integrating α-Fe_2O_3-based composite photoanode with better conducting materials [1,3], or by decorating the surface of α-Fe_2O_3 with a co-catalyst [1,3] to facilitate the oxygen evolution reaction (OER). Compared to the hydrogen evolution reaction (HER) at the photocathode (which is usually platinum), the four-electron transfer OER at the photoanode is the rate-limiting step in the overall process. Although hematite has an appropriate valence band edge (2.4 to 2.7 eV) for the OER in water oxidation, the conduction band minima (0.3 to 0.6 eV) is lower than the required value for the hydrogen evolution reaction (HER) [4]. Consequently, the development of a high efficiency photoanode is the critical step in designing improved devices.

The US Department of Energy recommends that a PEC device should cost less than US$ 160 per m^2 with a solar-to hydrogen (STH) efficiency of approximately 10% [3] (which is below the maximum theoretical efficiency of 15% calculated for many metal oxide photoanodes). [3]. The maximum theoretical STH efficiency of hematite is *ca*. 15% and substantially higher than the STH benchmark efficiency of 10% required for commercial applications [1,4-7]. However, to achieve such an efficiency practically, hematite needs to overcome issues such as low electrical conductivity, slow charge transfer kinetics at the electrode/electrolyte interface and a high overpotential. Since 1978 substantial research has been performed to understand the basis of these issues and to improve PEC performance as a result. The highest photocurrent density (J_{Ph}) reported for a pristine hematite photoanode was 1.26 mA cm^{-2} in 2013 [7]. The report describes a single-crystalline "wormlike" hematite film prepared on fluorine doped tin oxide (FTO) by first forming 1-D β-FeOOH nanorods and then converting them to α-Fe_2O_3 by a two-step annealing treatment at relatively higher temperatures of 500 and 800°C. The measured photocurrent is then further improved by the addition of oxygen evolution cocatalysts (Co-Pi) to modify the surface properties. The resulting hematite photoanode showed a PEC water oxidation current of 4.32 mA cm^{-2} at 1.23 V vs. RHE under simulated 1-sun (100 mW cm^{-2}) irradiation. The system could produce 555 µmol cm^{-2} of H_2 in 3 h.

The most recent reports of high J_{pj} values are those in which hematite is modified either by doping or through surface treatments [7-14]. Zhao et al. [11] used Ge as a dopant to obtain modified hematite films with a current density of 0.92 mA cm^{-2} while Zandi *et al* [9] adopted a strategy of titanium doping to improve the charge transfer characteristics of bulk hematite to yield 2.8 mA cm^{-2} at 1.23 V vs RHE. More recently, Liu *et al*. also added Ti, synthesizing doped ultrathin hematite photoanodes via a layer-by-layer polymer assisted deposition method to record a photoanode current density of 1.30 mA cm^{-2} [15]. Employing co-catalyst, nano-structuring and non-metallic doping approaches have also been adopted such as phosphorous doping considerably increased the current density upto 2.0mAcm^{-2}[14,16] and the decoration of hematite films with a FeOOH/NiOOH as dual cocatalyst also caused an improvement in the current density [17]. In a report in 2018, one-step in-situ synthesis of hematite–tungsten oxide (α-Fe_2O_3–WO_3) composite on fluorine-doped tin oxide (FTO) substrate was carried out via simple hydrothermal method. The obtained electrode could demonstrate water oxidation photocurrent density of just 0.80 mA/cm^2 (at 1.6 V vs. reversible hydrogen electrode under standard illumination conditions [13]. As the interfacial sites affect the properties of the photocatalyst therefore, interfacial layering of the hematite with different dopants and blends have been exploited for improved efficiency in recent years [18-19]. Processing routes have also become important in mediating film quality and

performance as with slight variations in structure or morphology often strongly influencing the light absorption and charge transport properties of the material. Aerosol-assisted chemical vapour deposition (AACVD) has proven to be very successful in producing high performance films. Tahir *et al* originally demonstrated the potential of this method, producing a hematite film with a photocurrent density of 455µA cm^{-2} at 1.23 V vs RHE [20]. Subsequently a current density of 585 µAcm^{-2} at 1.23 V vs. RHE was obtained in a hematite film by using AACVD method. [21].

In present work, we assessed the importance of processing techniques by synthesizing nanostructured α-Fe_2O_3 thin films via three different methods, namely: spray pyrolysis (SP), chemical vapor deposition (CVD), and AACVD. The thin films were fabricated into photoanodes on conducting glass substrates for structural and morphological characterization and for extensive, optical, electrochemical and photoelectrochemical testing. Systematic investigation of the effects of Fe^{3+} precursors, annealing temperature and solvent on film structure and quality enabled us to determine the optimum conditions for each processing method. The aim of the study was to develop pristine α-Fe_2O_3 photoanodes with improved surface properties so as to maximize the diffusion lengths of the PEC-generated charge carriers and enable fast carrier transport. The results showed that the AACVD method, in particular, can be employed to produce the quality thin films, which are evenly structured, with sufficiently large surface area, and which could reduce recombination rate and increase carrier diffusion lengths [22]. In this way, a substantial photocurrent density of 1.23 mA cm^{-2} could be achieved for pristine hematite without any doping or surface treatment through AACVD just at 525°C temperature. The hydrogen gas evolution reaction was indirectly monitored, and the yield of the gas was quantified.

2. Experimental

2.1 Materials Used

Iron acetylacetonate $(C_5H_8O_2)_3Fe$ (99.9%), ferric chloride 99% and ferric nitrate nonahydrate 99% (Aldrich), absolute methanol (Fisher Scientific) and ethanol (Alfa Aeser) were obtained commercially and used without further purification. Fluorine-doped tin oxide (FTO) (TEC 8 Pilkington, 8 Ω/square) was used as conducting glass substrate. Doubly de-ionized water (DDW), (MilliQ water, from Elga system) with a resistivity of *ca*. 18.2 M Ω cm was used for the preparation of solutions.

2.2 Procedures and methodology

Three methods namely, spray pyrolysis (SP), chemical vapour deposition (CVD), and aerosol assisted chemical vapour deposition (AACVD) were used for the thin film preparation. Texture-controlled nanostructured hematite thin films were fabricated by using iron (III) chloride as the precursor in either ethanol or methanol. The FTO glass substrates were cleaned ultrasonically prior to use for thin film preparations using ethanol, iso-propanol and acetone for 15 minutes each, in sequence, and then washed with de-ionized water to remove any remaining impurity before drying with compressed air.

2.2.1 Spray pyrolysis

The spray pyrolysis setup comprised of a syringe pump system (New Era Pump System NE-1000), an ultrasonic atomizer nozzle (Sonozap) 1 mm diameter and a vortex attachment. The cleaned FTO glass substrate was set on the hot plate at 150 °C so as to maximise the coverage from the syringe pump. Compressed air was passed through a vortex attachment at 4 L min^{-1} to generate a large plume of aerosol in order to achieve a uniform coverage of the FTO. The Fe_2O_3 photoelectrodes were prepared by spraying 5 ml each of methanolic and ethanolic precursor solutions of 0.1 M $FeCl_3$, $Fe(NO_3)_3 \cdot 9H_2O$ and $Fe(acac)_3$, respectively at 150 °C for 20, 25 and 30 minutes on to the FTO at a rate of 0.60 ml min^{-1} for 40 minutes. The resultant films (**Fig. S1)** were heated at different temperatures, 450 °C, 475°C, 500°C and 525 °C with a ramp rate of 25 °C h^{-1} to produce single phase, crystalline Fe_2O_3 material. The complete description of iron oxide thin films prepared by using different solvents, precursors and for different deposition times and temperatures is given in **Table SI**.

2.2.2 Chemical vapor deposition

In a typical CVD experiment, 20 ml of 0.1 M solution of $FeCl_3$ in ethanol was combined with 0.1 ml of acetylacetonate in a 50 ml round-bottom flask. An FTO substrate was placed in a tube furnace for each deposition experiment and air was used a carrier gas, at a flow rate of 130 ml min^{-1}. Different deposition temperatures between 450, 475 and 500 °C were employed across a series of experiments. Films were deposited from precursor solution for time periods of 10,15,20,25 and 30 min at fixed temperatures. The deposition temperature and time were monitored and programmed to control the morphology of the thin films. At least five films were fabricated for a given deposition time at each set temperature. A comprehensive information of variables is given in **Table SII**.

2.2.3 Aerosol assisted chemical vapor deposition

Nanostructured α- Fe_2O_3 thin films were deposited on FTO glass substrate by AACVD using $FeCl_3$ as precursor. The 0.1 M methanolic and ethanolic precursor solutions were each used to generate aerosols. Each aerosol was generated by means of a pneumatic collision generation method, using a TSI Model 3076 constant output atomizer, which typically generates 0.3 μm-sized aerosol droplets. A stream of compressed air running at 2 bar constant pressure during depositions was used to transfer the aerosol to the reaction chamber. Air was used as a carrier gas, at a flow rate of 150 ml min^{-1} and deposition temperatures between 450 °C and 525 °C were employed (in 25°C increments using a hot plate). Each film was deposited for a period of 20, 25 and 30 min. In addition to the hotplate thermometer, the temperature of the FTO substrate surface was also measured using an additional external thermocouple taking readings prior to and during deposition. The experimental details are given in **Table SIII** and the films produced are shown in **Fig. S1**.

2.3. Instrumentation and characterization techniques

An X'Pert PRO MPD diffractometer equipped with a monochromator, employing Cu Kalpha1 radiation was used to analyze the phase purity and crystallinity of the deposited films by powder X-ray diffraction (PXD). Diffraction data were collected in from 5.0027 to 84.9617 (minimum step size $2\theta = 0.001°$). Raman spectroscopy was performed with a Horiba LabRAM HR Raman microscope equipped with a Helium Cadmium IK3201R-F UV Laser (325 nm; 20mW) and a Ventus 532 visible laser (532 nm; 200 mW). All samples were run with 50x objective. Scanning electron microscopy (SEM) coupled with energy dispersive X-ray spectroscopy (EDX) was performed to assess the morphology and the elemental composition of the Fe_2O_3 nanocrystalline films. A MIRA 3 TESCAN instrument with SEM magnification 25.0kx and SEM HV 20.0kv,BI 9:00 are used for these experiments.

For optical characterization, a PerkinElmer lambda 1050 spectrophotometer equipped with a 150 mm InGaAs sphere was used to record diffuse reflectance and absorbance UV-visible spectra. Electrochemical, EIS and photoelectrochemical measurements were conducted using a typical three electrode set-up fitted with a quartz window. The electrode configuration comprised of various α-Fe_2O_3 thin film samples deposited on FTO as a working electrode, Ag/AgCl/3M KCl as a reference electrode and Pt wire as a counter electrode immersed in 0.1 M NaOH electrolyte (pH ~ 13). The measurements were made with a micro-Autolab, type III potentiostat/galvanostat set-up. An AM1.5

class-A solar simulator (Solar Light 16S-300) was used as an illumination source in photoelectrochemistry experiments. The electrode was illuminated through the electrolyte side utilizing an illumination area of 1 cm^2 and measurements were made at a scan rate of 0.01 Vs^{-1} scan rate both in darkness and in chopped light.

Gas chromatography (GC) measurements were made as described previously [23] and reproduced as such. "A manual injection GC system (PerkinElmer Clarus 580) using a molecular sieve (PerkinElmer) and a pulsed discharge detector (PDD) with an argon flow of 28 ml/min were used. A custom-made glass reactor vessel with an attached fused silica viewport containing 0.1 M NaOH (pH 13) with a dead space of 100 ml was purged with argon for 2 hours with gentle heating and stirring to remove atmospheric air from the system. No sacrificial agents were used. The sealed vessel contained the working Fe_2O_3 electrode connected to a Pt mesh by a single outer wire and was subjected to light illumination for the water splitting reaction. GC measurements were carried at an interval of 1 hour [23]".

3. Results and Discussions

3.1 Structural and morphological characterization

3.1.1 PXD analysis:

PXD analysis was performed on each of the film samples synthesized by SP, CVD and AACVD methods, primarily to ascertain phase purity of the anticipated α- Fe_2O_3 samples. The representative results are shown in **Fig.1** while others in **Fig. S2,** and **Table SIV**. It is apparent from peak pattern of all the α- Fe_2O_3 films, deposited by three methods on FTO substrate, that apart from dense SnO_2 diffraction peaks due to FTO at least three characteristic peaks of hematite, specifically (104), (110) and (300) are visibly present. In addition to these reflections some weaker peaks corresponding to the (012), (006), (113), (024), (116), and (122) planes are also observable. All the observed reflections are closely matched with the standard values (JCPDS-00-024-0072) of the inter-planar distance *d* for hematite [21] and are indexed to their respective Miller indices. The absence of some of the peaks may be due to very intense peaks of the substrate and slight 2θ shift for some of the peaks could be ascribed to the lattice mismatch between substrate and film which causes strain in the film lattice.

Among the films prepared via the three different synthesis methods, those produce by CVD most closely resemble the standard hematite diffractograms in terms of number of characteristic peaks and intensities **(Fig.S2**). The apparent slight mismatches in the line pattern are artifacts occurred while grouping all patterns in one figure. The PXD patterns

obtained were converted into line patterns because the peaks of α-Fe_2O_3 were suppressed by the reflections due to FTO substrate. The original PXD patterns of the films prepared from the three methods and by AACVD method at different temperatures are shown in **Fig.1.** The PXD patterns of the films prepared under different experimental conditions are available in supplementary data **(Fig.S2). Fig.1a,** represents PXD patterns of α-Fe_2O_3 formed by three methods at optimized conditions, wrt PEC performance (discussed alter), of precursor ($FeCl_3$), solvent, temperature, and deposition time.

Fig.1.

The PXD data for the films deposited at different temperatures are normalized to the high intensity FTO peak at 37.9°. Martínez et al. [24] reported the deposition of α-Fe_2O_3 films and found that structural properties such as crystallinity and phase purity are strongly dependent on the deposition temperature. The current analysis proved the same and appearance of no other iron oxide phase in the PXD patterns in **Fig.1** is suggesting the suitability of the procedures adopted for the preparations of pure α-Fe_2O_3 thin films using $FeCl_3$ precursor. The crystallite diameter (*B*) was approximated according to Scherrer's formula [25], as given below in equation 1, and the measured and calculated results are collated in **Table SIV**.

$$B\,(2\theta) = K\lambda / \beta \cos\theta \qquad \textbf{(1)}$$

where β is the full width at half maximum (FWHM) of each diffraction peak. A Scherrer constant of K = 0.9 was employed, consistent with a rhombohedral crystal system. Cu-Kα radiation was used throughout, with wavelength, λ = 1.5406 Å,.

Films obtained by the SP method gave crystallite diameters varying from approximately 5-20 nm for the corresponding temperature range of 450 ºC,475 ºC,500 ºC and 525 ºC in ethanol solutions, i.e., with a decrease in particle size on increasing annealing temperature. On changing the spray solvent to methanol, the crystallite size varied from approximately 3-23 nm over the same temperature range. However, in methanol solvent the variation in crystallite size was same in comparison to AACVD method. The film composition, surface morphology, deposition rate, and the internal structure are dependent on the momentum and thermal diffusivity of the carrier gas and as a result the mean free path and mass diffusivity of the reactant molecules are also affected on changing the carrier gas. It is observed in

other works that high thermal diffusivity and high molecular velocity of helium gas lowers the deposition rate due to the formations of intermediate species which can go out of the reactor [26], but this is not important here. The effect of precursor solutions was also investigated by SP method. It was found that the films prepared using Fe(accac) gave consistently smaller crystallite diameters (average values ranging 5 – 8 nm) in comparison to the sizes calculated for the films obtained from $FeCl_3$ and $Fe(NO_3)_3.9H_2O$ precursors.

A similar trend of decreasing crystallite size, with increasing temperature (425 to 525 ^oC) was also observed for films prepared by the CVD method. In this case, crystallites varying from approximately 5-23 nm were produced. For employing iron oxide as photoanode in photoelectrochemical water splitting a crystalline, nanostructured deposit is desirable [27-28]. As expected, the deposition temperature has a significant impact on the crystallinity of the films. Increasing the temperature to 600, 700, and 800 °C leads to additional and more intense reflections. Due to the low intensity of the reflections in the XRD patterns, it is difficult to assign the structures. The morphological appearance of the iron oxide deposits, beside its crystallinity, is of high impact considering the performance of the material in photoelectrochemical (PEC) water splitting. This means the CVD-grown Fe_2O_3 films essentially behave as conventional compact n-type semiconductors in which the efficiency-limiting factor is the short diffusion length of the minority charge carriers (holes).

Of the thin films prepared by the three different techniques employed, those fabricated by the AACVD method yielded diffraction patterns with the strongest resemblance to that hematite (ICDD PDF 00-24-0072), with characteristic peaks corresponding to the (012),(104),(110),(116),(214) and (300), reflections (**Fig. 1**). The sharp and intense peaks indicate the presence of pure crystalline alpha phase hematite (α-Fe_2O_3). The calculated crystallite size is in the range of 6 to 7nm. In the films by AACVD method the higher intensity of the (104) and (110) peaks indicate that the α-Fe_2O_3 particles are orientated in the said directions. For water splitting application it is a favorable result because the conductivity of α-Fe_2O_3 along the (110) direction is higher than that in the orthogonal direction [27- 28]. Most of the peaks correspond to Fe_2O_3 are indexed to rhombohedral system (JCPDS 00-024-0072). The intensity of the peaks increases with temperature and the peak at (214) is shifted towards left i.e., lower 2θ value whilst the rest of the peaks are shifted slightly towards higher 2θ values in comparison to reference hematite. The peaks for 475°C sample are diminished, therefore the FTO peaks are also not apparent.

Comparing among the three preparation methods it is apparent that the crystallite size of the films obtained from the AACVD method is smallest and provides the least variation on changing the film processing temperature. The observed change in morphology with the increase in temperature is attributed to the gradual shift of nucleation from heterogeneous to homogeneous process. The mechanism of AACVD deposition and the effect of homogeneous or heterogeneous nucleation on the texture and morphology of thin films has been discussed in detail elsewhere [20] The PXD patterns of the full set of films prepared by the three methods at 475 °C and 500 °C are shown in **Fig S2**.

3.1.2 Raman analysis:

A typical Raman spectrum of a α-Fe_2O_3 film consists of clearly visible bands at 225, 245, 291, 411, 500, 611 and 1321 cm^{-1}[29]. Hematite crystallizes in the D^6_{3d} space group and seven bands are expected in the Raman spectrum. As shown elsewhere, the Raman spectrum of an α-Fe_2O_3 film on FTO substrate is dominated by two A_{1g} modes at 225 cm^{-1} and 500 cm^{-1}, and three E_g modes at 299.7 cm^{-1}, 399.8 cm^{-1} and 607.6 cm^{-1} [30]. Additionally, FTO substrate bands can also appear in experimental spectra. In many cases, it is reported that a band at *ca*. 245 cm^{-1} is visible on the flank of the 225 cm^{-1} peak [30]. From the literature, a further band at approximately 1305.7 cm^{-1}, can also be observed, which is associated with a vibration of unclear origin [29]. De-Faria et al. [31] suggest that this band is caused by the scattering of two magnons in the structure, but according to Su et al. [32], the band is a second harmonic vibration.

Fig. S3 compares the Raman spectra of α-Fe_2O_3 thin films on FTO after annealing at different temperatures for 30 min in ethanol, as prepared by all the three methods. The characteristic two A_{1g} (222 and 498 cm^{-1}) and five E_g (225 cm^{-1}, 243 cm^{1}, 290 cm^{-1}, 408 $cm^{-1}$and 608 cm^{-1}) bands are clearly visible in all the spectra. Considering first the results obtained for the CVD films, the experimental spectra are very much consistent with those reported for α-Fe_2O_3 across the measured Raman shift range. All the expected hematite bands are present, albeit broadened in comparison to the others reported previously [31]. In most cases, the 225 cm^{-1} band in the experimental spectra is flanked by the 245 cm^{-1} band.

The Raman spectra of hematite films prepared by SP methods also showed the characteristic seven bands across the measured Raman shift range: specifically the two A_{1g} modes (226 cm^{-1} and 497 cm^{-1}) and the five E_g modes (245 cm^{1}, 292 cm^{-1}, 298 cm^{-1}, 412 cm^{-1} and 613 cm^{-1}). The position of the peaks is in good agreement with literature data. Among

the three precursors used in the SP experiments, $FeCl_3$, $Fe(NO_3)_3.9H_2O$ and Fe(acac), the distinct sharp peaks with different intensities were of the films from the $FeCl_3$ [30] .

The Raman spectra of α-Fe_2O_3 prepared by AACVD at different temperatures in ethanol and methanol respectively for 30 minutes deposition time are shown in **Fig. 2a &b.** The respective spectra demonstrate all the characteristic peaks expected for α-Fe_2O_3, with the two A_{1g} mode bands at 224 cm^{-1} and 495 $cm^{-1}$and three E_g mode bands at 189 cm^{-1}, 289 cm^{-1}, and 412 cm^{-1}. Besides the typical A_{1g} and E_g symmetry phonon modes (below 620 cm^{-1}), a very strong feature was also detected at 1315 cm^{-1} when the spectral range was extended to 1500 cm^{-1}, which as discussed above, could be attributed to a second order phonon-photon interaction, [33]. In ethanol peaks at 475C are more prominent than at other temperatures, however, in methanol there is not much change in spectra for films annealed at various temperatures. A sudden jump below 500cm^{-1} for ethanol-based films could not be ascertained.

Fig. 2.

3.1.3 SEM analysis

The SEM images of the SP hematite films prepared at 525 °C are presented in **Fig. 3(a)**. From the images it is apparent that the surface of the films prepared by the SP method is composed of dense, irregular, and uneven pattern of agglomerates/clusters of different sizes ranging from 90 - 550 nm and an average particle size of 180 nm which is in good agreement with the SEM images reported in the literature [34-35]. The SEM images also show that the sintered microparticles are effectively non-porous.

A representative SEM image of a film prepared by the CVD method at a temperature of 525 °C is shown in **Fig3b**. The film has a very distinct morphology with sub-micron sized platelets clearly visible. These platelets are of sizes ranging between 0.5 to 1 µm in length, 100 to 150 nm in width and less than 50 nm in thickness. The coverage of the film surface is homogenous with an approximately uniform distribution over the entire surface. Each of the platelets appears to be smooth. The CVD-deposited films exhibit a higher internal surface area in comparison to those prepared by the SP method owing to have smaller particles.

Fig.3(c) shows the SEM image of hematite thin films deposited for 30 mins at 525°C using $FeCl_3$ in methanol via AACVD. The particle morphology is very similar to that obtained by CVD but with platelets of a much smaller size

(i.e., of length 250 - 300 nm). The width of the flakes is also in the nano-range (i.e., 60 – 100 nm), while the thickness is approximately 20 – 30 nm; about half that the platelets obtained by the CVD method. As the SEM image for the AACVD thin films is a bit blur therefore, the thickness of the platelets is a projected value based upon the length and width values. This in analogous to CVD results. From the variation in the dimensions of the particles it is speculated that the nanoparticles cluster up, however this needs further investigation and could be an interesting study. **Fig.3(d)** gives an estimate about the thickness of the film through cross sectional image.

All the α-Fe_2O_3 films adhered well to the FTO substrate regardless of preparation method and in each case the thickness of the film (typically from 0.475 to 0.91µm) showed a linear dependence with the deposition time. The films prepared by SP, CVD and AACVD, using methanol solvent and annealed at 525^{o}C, showed an average thickness of 0.745 µm, 0.91 µm and 0.475 µm thickness, respectively. The effect of the shape and size of the component particles is discussed with respect to the PEC performance of the films in later sections.

Fig. 3.

The EDX spectra taken of all the films confirm that there are no other elemental impurities in the prepared films and the theoretical and experimental ratios of the constituent elements (2:3 Fe:O) complement each other (**Fig. S4** shows each of the EDX spectra of the films in sequence). In view of the structural and morphological studies of the films prepared by three methods it was recognized that the films prepared by AACVD method are best and hence used for further property characterization studies.

Here the deposition time is affecting the thickness of the film which then affects crystalline structure, band gap, and absorption intensity of the films. To observe the effect of temperature on the XRD patterns of the films developed from three different methods, i.e., SP, CVD and AACVD, the deposition time was kept constant, and temperature was varied. The obtained results, **Table SIV**, clearly show that the crystallite size is found to decrease with the increase in temperature for SP and CVD methods but for AACVD it remains same. Grain size of the films by SP and AACVD at 525°C, given in **Fig.3**, is in nanoscale range, and the cross-sectional image of the film formed by AACVD (**Fig.3d**) indicates it is thinnest (0.475µm), though the thickness of films by other two methods is also less than 1 micrometer.

Referring to **Table SVI,** it is obvious that change in Eg is not following a much regular pattern with the change in temperature probably due to partial structural variation.

3.2 Optical and electrochemical characterization

3.2.1. Optical analysis -UV- Visible spectroscopy

The optical analysis was conducted on hematite thin films prepared by the AACVD method. **Fig. 4a** shows the absorption spectra of hematite thin films prepared by using $FeCl_3$ and methanol as solvent for 30 minutes at different temperatures. It is apparent that the absorption is negligible above 650 nm and as the wavelength continues to decrease, there is a marked increase in absorbance, which reaches its maximum value at approximately 530 nm. The artifact observed at 380 nm is due to a change of the light source in the spectrophotometer. Increasing the preparation temperature of the films does not result in any significant shifts in the position of the maxima or other features. Otherwise, the spectra are consistent with those previously reported for pure hematite films on an FTO substrate [34-35]. Considering the films prepared by the AACVD method at 550°C in methanol, an λ_{max} value of 540 nm is observed and the corresponding value of the absorption coefficient (α) can be calculated by using the measured film thickness of 0.475 µm) (as obtained from cross sectional SEM imaging) and by applying the following formula [34]:

$$\alpha = 2.303\,(A/d) \qquad \textbf{(2)}$$

Where *A* is the absorbance, 0.473 at 540nm, and *d* is the diffusion length. This yields of value of the absorption coefficient, $\alpha = 2.293 \mu m^{-1}$.

It has been reported that the lifetimes (of a few ps) and diffusion lengths (of *ca*. 2–4 nm) of the charge carriers in hematite photoanodes are short and that charge recombination is probable (either at the surface or in the bulk) [35]. These phenomena impair the PEC performance of hematite photoanodes considerably and so a focus has been placed on the microstructural tuning and surface treatments of such thin films to minimize carrier recombination [36].

Fig. 4.

The optical bandgap (E_g) was calculated according to the following equation:

$$\alpha h\nu = A^{\circ}(h\nu - E_g)^n \qquad \textbf{(3)}$$

where α is the absorption coefficient, hν is the photon energy in eV, and E_g is the band gap energy in eV. A° and n are constants that depend on the kind of electronic transition, n being equal to 1/2 and 2 for allowed direct and indirect transitions, respectively. **Fig.4b** shows the Tauc plots of $(\alpha h\nu)^2$ versus photon energy hν for α-Fe_2O_3 films deposited by AACVD for 30 min at different temperatures. The calculated bandgap of 1.99 approximately 2.00 eV was estimated from the intercept by extrapolating the linear fit of the Tauc plot to the energy axis of the film deposited at 450°C in methanol for 30min deposition time. The observed linear part of the Tauc fit indicates that the Fe_2O_3 electrodes deposited from methanol at 525 °C have a direct band gap of 1.94 eV as shown in **Fig. 4b.** The estimated bandgaps of 1.9 - 2.1 eV agree with the reported bandgap values for α-Fe_2O_3 [20, 37]. As films are deposited under varying conditions of solvent, deposition time and temperature, so the crystallinity and thickness of the Fe_2O_3 films will vary which will also impact on the optical absorption edge and bandgap [38]. The variation in film thickness affects the localized energy states which in turn changes (slightly increases or decreases) the bandgap of the material. The AACVD thin films prepared in methanol **Fig.4b** showed a slight red shift with increasing temperature for 30 min deposition time, which possibly indicates the creation of additional energy states at higher temperature.

The absorption coefficient value can be calculated from the diffuse reflectance using the Kubelka–Munk equation given below:

$$F(R) = \frac{(1-R)^2}{2RS} = K \qquad \textbf{(4)}$$

where, *R* is the absolute reflectance of the hematite nanoparticles, *K* is the molar absorption coefficient and *S* is the scattering coefficient [39]. The obtained DR-UV-Vis spectrum is converted to the Kubelka–Munk function F(R)such that the vertical axis represents the quantity $[F(R)\,h\nu]^2$, which is plotted against photon energy (hν) as shown in the **Fig. 4c**. The linear part of the curve is extrapolated, and the optical band gap energies of the films were obtained from the energy intercept, yielding values in the range of 2.05 and 2.08 eV for 20min and 30min deposition times, respectively (**Fig.4c** and inset). The calculated band gaps for the films prepared using methanol or ethanol as solvent are collated in **Table SVI.** As can be seen from **Fig. 4(c),** an apparent blue shift is observable in the reflectance spectrum of the films moving from 20min to 30min deposition time. Further, in case of ethanol solvent, increasing the preparation temperature from 450°C to 475°C leads to a decrease in the band gap from 2.08 to 1.98 eV, for 20min deposition time. However, for the films prepared for 30 min, the band gap increases from 1.97 to 2.08eV as the temperature is increased from 450 °C to 525 °C. Tauc and Kubelka-Munk plots for other films are shown in **Fig. S5.**

3.2.2. Photoelectrochemistry- linear sweep voltammetric analysis in in the absence and presence of light

The photoelectrochemical performance of the prepared α-Fe_2O_3 films was studied by recording the photocurrent density as a function of applied voltage. The experiment for all the three type of films (SP, CVD and AACVD) were performed in the dark, in continuous light and in chopped light at regular intervals. For the latter two types of experiments a source of simulated solar illumination (AM 1.5 G) under 100 mW cm^{-2} was used at 25 °C. The steady state J–V plot was superimposed on the transient plot in each case for comparative analysis. Generally, the dark current onset begins at approximately 1.7 V vs. RHE for all the electrodes in a 0.1 M NaOH electrolyte. The amount of dark current was observed to decrease with increasing film deposition temperature. The characteristic potentials at which current starts were calculated employing Nernst's equation, as reproduced below:

$$E_{RHE} = E_{Ag/AgCl} + 0.059pH + E^{0}_{Ag/AgCl} \quad \textbf{(5)}$$

where E_{RHE} is the converted potential vs. RHE, $E°_{Ag/AgCl}$ = 0.197 V at 25 °C and $E_{Ag/AgCl}$ is the experimentally measured potential against Ag/AgCl [34].

A systematic and comprehensive study was performed in order to obtain a full understanding of the behaviour of each type of film. The SP films considered were obtained from three different precursors -$FeCl_3$, $Fe(NO_3)_3.9H_2O$ and $Fe(acac)_3$ - using either methanol or ethanol, each at a deposition time of 30 min and by employing temperatures of 475°C, 500°C and 525°C (Supplementary Information; Fig. S5 and S6). **Fig. 5a-d** show the results obtained at 525°C for the three precursors in each solvent. The PEC performance of various ironoxide films along with the complete experimental conditions is given in **Table SVII**. The results show that in films from SP the photocurrent increases for all the films with different thicknesses. It has been demonstrated earlier that regulating the film thickness can balance photon absorption and charge carrier transport in order to reach higher PEC performances [39-40]. Owing to short hole diffusion length in α-Fe_2O_3 (2–4 nm), it is necessary to decrease the film thickness but decreasing film thickness may result in loss of light absorption.

Fig. 5.

It is apparent that under dark conditions the onset potential for almost all of the SP films is beyond 1.6V in both the solvents. However, in the presence of simulated sunlight (**Fig. S6)**, films fabricated from $FeCl_3$ in ethanol at a fixed deposition time at different temperatures exhibited a reduction in onset potential, with values between 1.4-1.5V. On using other precursors under similar conditions, the changes in onset potential were not substantial; $Fe(NO_3)_3.9H_2O$ gave values of 1.49-1.56 V and $Fe(acac)_3$ yielded a potential onset at 1.6 V . On switching from ethanol to methanol (with all other parameters constant) the onset values tend to be lower i.e., 0.49 V - 1.45 V for $FeCl_3$, 0.55 V - 1.44 V for $Fe(NO_3)_3$ and 0.61 V - 1.54 V for $Fe(acac)_3$. The shifts in onset potential towards less positive values at 525°C should prove beneficial for energy harvesting. To gain a better understanding of the photocurrent behaviour in films prepared under different conditions, the LSV experiments were performed under chopped light with the results shown in **Fig.5b, 5d**. From these results, the films deposited using ethanol produce a photocurrent density in the range of 0.001 - 0.05 mA cm^{-2} , 0.009 - 0.03 mA cm^{-2} and 0.005 - 0.023 mA/cm^2 for $FeCl_3$, $Fe(NO_3)_3.9H_2O$ and $Fe(acac)_3$, respectively, for three different temperatures. Notably, the current density reaches substantially higher values for the $FeCl_3$ -produced film in comparison to the films prepared from the other precursors. The current density further increases when methanol replaces ethanol, particularly for $FeCl_3$ films. The respective current density values for the films are, 0.015 mA cm^{-2}, 0.063mA cm^{-2} and 0.12mA cm^{-2} at 475, 500 and 525°C, respectively.

Fig. 6.

The representative films shown in **Fig.6** prepared by CVD methods at 500°C at different deposition times using a $FeCl_3$ precursor in either ethanol or methanol. The onset potential in the presence of light is in the range of 1.01 V - 1.17 V, with the lowest onset potential obtained from films prepared using the longest deposition period and ethanol as a solvent. A possible reason could be the passivation of surface trap states by high temperature heating treatment [23]. When studied under chopped light, the photocurrent produced by CVD films made using ethanol (Fig..6b), is found to be increase with temperature, with a maximum photocurrent of 0.123 mA cm^{-2} at 1.23 V vs. RHE. Improvements in the PEC for the films treated at higher temperatures are attributed to the improvement in crystallinity of the hematite films. Further, the annealing the films at higher temperature improved the optical absorption, as recorded above in section 2.3, which in fact is because of film densification process causing more absorption of incident photons [41]. The temperature treatment of the film decreases the inter particle distance and thus favours the electron movement, probably the electron hoping [42]. A film annealed at higher temperature provides a conduit net

which decreases the hindrance to the generated free electrons and holes and increases intrinsic carrier population which helps in fast charge transport and better conductivity. However, at the same time the agglomeration of particles also increases with increase in temperature and after certain value it may affect the PEC efficiency adversely [43].

The J-V behavior of all the rest of the prepared films prepared is shown in **Fig. S6 and Fig. S7.**

The highest photocurrent produced by any of the photoanodes prepared using methanol was approximately 0.29mA cm^{-2} at 1.23 V; i.e., more than twice that observed form similar films produced using ethanol, which indicates substantial difference in performance are imbued by switching solvent. This can presumably be explained by a complex interplay of several factors in the fabricated films, such as faster surface kinetics, improved current collection and/or enhanced light absorption. It has already been reported that methanol minimizes the surface roughness of deposited hematite films and produces smaller and smooth regular pattern of the particles [44]. Possibly this also reflects the facilitation of the formation of oxygen vacancies and consequently increases the electrical conductivity due to a greater number of photogenerated electron-hole pairs.

Fig. 7.

The photoelectrochemical performance of nanostructured α-Fe_2O_3 films prepared by AACVD at 475°C,500C & 525°C for deposition times of 20, 25 & 30 minutes in ethanol and methanol solvents using $FeCl_3$ as a precursor, was subsequently investigated. It was observed that an increase in both the deposition temperature and deposition time increases the steady-state photocurrent density.

The steady state currents in darkness and under full illumination were recorded (LSVs) for the films fabricated using ethanol at a fixed temperature with different deposition time periods as shown in **Fig. 7**(a). Generally, the dark current starts at *ca*. 1.7 V for all the electrodes in 0.1 M NaOH electrolyte. For all the electrodes prepared with ethanol over a 30 min deposition time, the photocurrent increased rapidly with onset potentials of 0.83 V,0.98 V and 0.89 V at 475°C, 500°C & 525°C, respectively (**Fig. S6**). LSVs show that for methanol-prepared films under illumination and in darkness (Fig. 7(c)), the onset potential varies from 0.75 V to 0.96 V, with the lowest potential of 0.75 V at 525°C. This corresponds to an 8.4% decrease in the onset potential as compared to films prepared with ethanol (**Fig. S6**).

In the methanol-prepared AACVD films the photocurrent increased from 0.047 mA cm^{-2} to 0.335 mA cm^{-2}, from

0.045 mA cm^{-2} to 0.673 mA cm^{-2}, and from 0.079 mA cm^{-2} to 1.23 mA cm^{-2} for processing temperatures of 475°C, 500°C & 525°C, respectively (Fig. S6). The respective current density values are 0.106, 0.24 and 1.13 mA cm^{-2} for the films prepared in ethanol (**Fig. 7(b)**). From **Fig.7(d)** it is apparent that the electrode deposited at 525 °C, prepared using methanol delivered the highest current density of 1.23 mA cm^{-2} at 1.23 V. Importantly, this value also represents the highest photocurrent density recorded among any of the hematite films, irrespective of preparation method (i.e. SP vs. CVD vs. AACVD). This increased photocurrent density at 525 °C can take values of 1.23 -1.32 mA cm^{-2} when the potential is raised from 1.23 V towards 1.27 V. The observed photocurrent maximum can be interpreted in terms of a large active surface area due to smaller particles and hence a more effective semiconductor for photoelectrochemical cell. The photocurrent data for the remaining films are provided in the supplementary information (**Fig. S7**). In very few samples the photocurrent in continuous light was found higher than that of the same film in chopped light which was attributed to surface changes during the experiment. However, the calculations are always based on lower photocurrent values.

The evidence of the higher photocurrent that can be obtained at higher potentials for films deposited over 30 mins (e.g., 1.23mA cm^{-2} at 1.23 V and 1.32mA cm^{-2} at 1.27 V when using methanol and heating at 525°C) clearly shows the importance of deposition time. This is ascribed to the improvement in film structure leading to higher crystallinity as indicated by PXD analysis. One would expect these well sintered, denser, crystalline films to exhibit superior transport properties. The resulting α-Fe_2O_3 film morphology also provides a better interface between the electrode and the electrolyte for rapid charge transfer. The relevant diffusion distances are sufficiently short for the photogenerated holes to reach the electrolyte rapidly, suppressing their recombination.

The observed increase in photocurrent with the increase in film deposition temperature tends to indicate further improvements in film structure. At higher processing temperatures there would be a greater driving force to reorient adjacent grains of hematite and to remove grain boundaries, thus further facilitating electronic transport within the hematite film. In fact, the photocurrent density of the optimized AACVD α-Fe_2O_3 thin films (of 1.23mA cm^{-2} at 1.23 V vs. RHE) is to the best of our knowledge, the highest photocurrent reported to date for any pristine (externally un-doped) hematite thin film prepared by the AACVD method. By comparison, a photocurrent of 455μA cm^{-2} at 1.23 V vs. RHE at 450°C was reported for a nanostructured α-Fe_2O_3 AACVD thin film in 2014 [20], while in 2019, a current density of 585 μA cm^{-2} at 1.2 V vs Ag/AgCl was recorded for an AACVD hematite film [21].

This impressive PEC performance of AACVD thin films would seem to be generally attributable to the improved crystallinity of hematite nano-elliptical thin films with enriched (110) facets (Fig. 1a & b) and their consequent excellent light harvesting property. Despite a hole diffusion length of the order 2–4 nm [21] the tuning of the thin film nanostructure substantially affects the photocurrent. The electron-hole (e-h) separation within the width of the space charge layer becomes a key factor, which seems to be more pronounced for electrodes composed of films deposited at higher temperature (in our case, at 525 °C). **Table SVII** compares the PEC performance (e.g., in terms of lowest onset potential and highest photocurrent density at 1.23 V vs. RHE) of an extended selection of photoanodes with respect to fabrication method and key processing parameters.

The stability of the prepared photoanode in PEC water splitting is crucial for both fundamental and practical studies **Fig. 7e** contrasts the photocurrent curves of optimized AACVD α-Fe_2O_3 photoanodes fabricated with either methanol or ethanol measured at 1.23 V *vs.* RHE in a 0.1 M NaOH electrolyte under AM 1.5 illumination for 2.7 h. Although the photocurrent of the α-Fe_2O_3 photoanode varies from 0.145 mA cm^{-2} to 0.283 mA cm^{-2} and from 0.78 mA cm^{-2} to ~1.08 mA cm^{-2}, in ethanol and methanol, respectively there is no steady decline with time; in fact the current density fluctuates in a rather irregular manner. After 2.7 h the photocurrent is more than 90% of the initial value indicating that despite the observed fluctuations, both photoanodes exhibited very satisfactory stability during PEC water splitting.

The observed slight decrease in initial current density over time could be due to gas bubble accumulation, which was observed on the surface of the electrode during the test. The gas bubbles tend to adhere to the electrode surface, thus decreasing the effective available electrode area and increasing the interfacial electric resistance [45], which causes a decrease in current density. Further, a reduction in photocurrent density could arise from space charge accumulation on the surface of the film which creates a barrier to the reaction by preventing the charges accommodated by the electrolyte.

3.2.3. Electrochemical impedance spectroscopy (EIS) - charge transport dynamics

Charge transport kinetics and the interfacial dynamics were analyzed using EIS measurements performed on bare hematite photoanodes in order to try to understand the phenomena, such as deviations in photocurrent density, that we had observed. **Fig. 8 (a &b)** shows the impedance spectra obtained for the PEC cell in a three-electrode configuration

both in darkness and under illumination, the inset shows the actual shape of the spectrum in light for small impedance region. The spectra were analyzed in terms of charge transfer at the electrode-electrolyte interface.

On comparison of the Nyquist plots made from data taken in darkness and under illumination (**Fig 8a**) it is apparent that quite different impedance responses were obtained. The plot of data taken under illumination shows a semicircle (see the inset in Fig.8a) for the bare photoanode with much reduced impedance, negligible compared to the equivalent date collected in darkness. Generally, the high frequency semicircle describes the charge-transfer process in the semiconductor depletion layer and estimates the trapping of the photogenerated charges in the bulk of photoanode. By contrast, the semicircle in the low frequency region can be attributed to the electron transfer at the Helmholtz layer associated with the phenomenon of a change in surface states [46]. A decrease in the resistance of the α-Fe_2O_3 films in light indicates the ability of the electrode to produces a far higher current that is sufficient for water splitting. The noisy feature in the low frequency region of Bode plot is likely due to the surface morphological changes of the films.

It is well established that a space charge layer can arise between an electrolyte solution and a semiconducting electrode in an electrochemical cell under conditions of darkness [47]. An equilibrium between the electrochemical potentials of the two phases is established owing to the charge transfer process across the interface. The development of a positive space charge layer against the negative charge layer at the two sides of the electrode-electrolyte junction leads to the development of a depletion layer. This creates a potential gradient on the semiconductor side due to the arrangement of ions in the Helmholtz layer that develops. Upon illumination, photons with a threshold energy (greater than the band gap) absorbed on the surface produce e-h pairs. Those absorbed in the depletion layer are also able to generate e-h pairs by means of electric field generation. Consequently, the Fermi level of the semiconductor shifts towards its flat-band potential to attain its original equilibrium [48].

The corresponding Bode plots are shown in **Fig. 8b,** depicting the typical phase angle and total impedance profile versus scanned frequency range. The higher frequency peak in the Bode-phase diagram corresponds to the depletion layer, whereas the peak at lower frequency corresponds to the Helmholtz layer. The electrolyte layer adjacent to the solid/liquid interface which corresponds to a much lower impedance compared to that of the bulk [48], is analyzed.

Fig. 8

due to its involvement in the photocurrent generation. In darkness, the diffusion of ions within the electrolyte solution is a mass transport process and is indicated by a Warburg element in the equivalent circuit of the EIS pattern [49]. Under illumination the mass transport is no longer based on a Nernst diffusion process; therefore, it cannot be modeled by a Warburg impedance. The absence of a linear contribution to the impedance at low frequency in the Nyquist plot (as a 45° diagonal line), also suggests the absence of mass transport. In darkness the observed higher resistance is due to the equilibrium of charges but in simulated sunlight the produced electrons pass to the external circuit due to the photoexcitation of the conduction band electrons which show very low negligible resistance as is evident from the impedance spectrum.

The Bode plot of the modulus impedance clearly depicts a decrease in resistance on moving to the high frequency region. Looking at the phase spectrum, two processes can be recognized in the lower and higher frequency regions, respectively. Namely the charge transfer at the solid/liquid interface (Helmholtz layer) and the charge transport inside the film (depletion layer). The increase in voltage accelerates the charge transfer and is reflected in the peak shift toward higher frequencies and is finally comparable with that of the other process for potentials larger than 0.6 V vs. Ag/AgCl (the onset potential). The facilitation of charge transfer process at higher potential is ascribed to the increase in surface states which can be interpreted as the charge transfer mechanism [48-50].

To generate a quantitative interpretation of the charge carriers produced, the electron lifetime (τ_e) was calculated from equation (6) below [51]. The electron lifetime (τ_e) in the pristine hematite films was thus obtained from the characteristic angular frequency (ω_{mid}) of the middle frequency (f_{mid}) peak in the Bode phase plots.

$$\tau_e = (1/(2\pi\omega_{mid}) \qquad \textbf{(6)}$$

An electron lifetime of 175 µs was obtained for the film prepared by AACVD method in methanol at 525Cin 0.1M NaOH. The lifetime is considerably higher than the majority of previously reported values which are typically in the range of 2 to 2.5 µs [52]. A very notable exception, however, is presented in the recent work by Subramaanian et al. where an electron lifetime of 1.09 ms was demonstrated to exist. This extraordinary electron lifetime possibly originated from the surface treatment of FeOOH and by employing the significantly higher film annealing temperature of 800 ^{o}C [53].

3.3. Hydrogen evolution measurements:

Fig. 8c shows the hydrogen generation performance of the Fe_2O_3 photoelectrode in an aqueous 0.1 M NaOH solution under constant illumination. The photoelectrochemical water splitting was monitored in a custom-made glass reactor vessel attached to a fused silica viewport as described in the experimental section. The hematite photoanode, which acted as the working electrode, and the Pt counter electrode were connected directly by a single looped wire, without any external bias. Gas evolution measurements was performed for several selected films prepared by AACVD methods and optimized results are shown in **Fig. 8c** above. Further data are reported in **Table SVIII**.

The observed amount of O_2 evolved is less than expected probably due to unanticipated gas leakage during the sampling and manual injection into the GC. Secondly, being the limiting nature of the oxygen reduction reaction (ORR), which accompanies with hydrogen evolution reaction (HER) on cathode surface could also be a reason for this decrease. Nevertheless, most of the photogenerated holes were consumed for oxygen production in the PEC setup. The amount of oxygen gas produced spontaneously from water splitting at the α- Fe_2O_3 photoanode was quantified for the first 6 h cycle as 1.2 μmol cm^{-2} while the corresponding amount of hydrogen evolved was 0.4 μmol cm^{-2} (**Fig.8c**). By way of comparison, in 2018 hematite nanorods annealed in Argon gas at 500 °C produced 45 μmol cm^{-2} of oxygen gas in 2 h [16], whereas in 2019, a Ti-modified hematite photoanode produced 2.5 μmol cm^{-2} of oxygen in 3 h [37].

There is an obvious correlation between the considerable amount of hydrogen produced by the electrode and the significant photocurrent that it produces (as seen in the J-V curves); enough electrons are generated to produce relatively abundant hydrogen. That the amount of hydrogen evolved was not even higher suggests that some of the generated electrons may not have been able to contribute to the production of hydrogen gas due to competing recombination processes. Two probable reasons for the decreased hydrogen generation could be: (a) that the dense morphology of the films adversely affected the penetration of the electrolyte into the film and (b) that bubbles accumulate as they form at the photoelectrode. These bubbles adhere to the electrode surface, decreasing the effective surface area and introducing additional surface resistance, thus increasing the chances of charge recombination. Both these issues are worthy of further investigation and should accordingly be addressed by appropriate surface treatment of the thin films.

4. Conclusions

Thin films of pristine hematite (α-Fe_2O_3) have been developed by three different deposition techniques, i.e., SP, CVD, and AACVD, as photoanodes for electrochemical water splitting. The results of PXD, RAMAN and SEM manifestly showed that single phase films could be obtained at 525°C with no evidence of undesired impurity phases such as Fe(II)-containing FeO and Fe_3O_4. The films prepared by the AACVD method produced remarkably high photocurrent density compared to the films prepared by the other two deposition methods. Moreover, to the best of our knowledge, optimized AACVD photoanodes (produced at a relatively low temperature of 525 ^oC) were able to generate the highest photocurrent density of any pristine hematite thin film reported to date (of 1.23 mA cm^{-2} at 1.23 V vs. RHE) with an onset potential approximately twice as low as any previous equivalent electrode. Encouragingly, the photoanodes prepared by SP and CVD methods also showed improved photocurrent generation in comparison to many previously reported pristine hematite electrodes prepared using similar methodologies. The selected thin film electrodes showed a 92% retention of photocurrent after continuous exposure to light for 6 h, thus demonstrating competitive photoelectrochemical stability. Electrochemical impedance spectroscopy revealed low electrical resistances and fast charge transfer kinetics on these films suggesting that photogenerated holes and electrons could diffuse to the electrolyte interface considerably faster than they could recombine. The photoelectrochemical generation of oxygen (1.2 μmol cm^{-2}) on the photoanode and that of hydrogen (0.4 μmol cm^{-2}) on the Pt counter electrode was established qualitatively and quantitatively over a 6 h duration.

Future work: In the continuity of this work the study of surface properties and doped analogues (e.g. TiO_2, C) of the α-hematite cold be an interesting research with AACVD method. Work is in progress in our lab on these lines.

Acknowledgment: We are very grateful to the Higher Education Commission (HEC) of Pakistan for financial support through a 6-month scholarship to S.Qureshi to visit the University of Glasgow under the International Research Support Initiative Program (IRSIP; No. *1-8/HEC/HD/2017/8222*).

Conflict of interest: The authors declare that they have no conflict of interest.

References:

1. A. G. Tamirat, J. Rick, A. A. Dubale, W. N. Su, B. J. Hwang, Using hematite for photoelectrochemical water splitting: a review of current progress and challenges. Nanoscale Horiz. 1, 243 (2016).
2. S. Y. Tee, K. Y. Win, W. S. Teo, L. D. Koh, S. Liu, C. P. Teng, M. Y. Han. Recent progress in energy- driven water splitting. Adv. Sci. 4, 1600337 (2017).
3. P. S. Bassi, T. Sritharan, L. H. Wong. Recent progress in iron oxide based photoanodes for solar water splitting. J. Phys. D Appl. Phys. 51, 473002 (2018).
4. T. Liu, M. Morelli, Y. Li. Photoelectrochemical Solar Cells, ed. by N.D. Sankir, M. Sankir (Wiley, Beverly, MA, 2018), p.159.
5. K. Sivula, F. Le Formal, M. Grätzel, Solar water splitting: Progress using hematite (α- Fe_2O_3) photoelectrodes. ChemSusChem. 4,432, (2011).
6. P. S. Bassi, L. H. Wong, J. Barber. Iron based photoanodes for solar fuel production. Phys. Chem. Chem. Phys. 16, 11834 (2014).
7. J. Y. Kim, G. Magesh, D. H. Youn, J. W. Jang, J. Kubota, K. Domen, J. S. Lee. Sci Rep. 3, 2681 (2013).
8. R. Zhang, L. Yang, X. Huang, T. Chen, F. Qu, Z. Liu, & X. Sun. Se doping: an effective strategy toward Fe_2O_3 nanorod arrays for greatly enhanced solar water oxidation. J. Mater. Chem. A 5, 12086 (2017).
9. O. Zandi, B. M. Klahr, T. W. Hamann. Highly photoactive Ti-doped α- Fe_2O_3 thin film electrodes. Energ. Environ. Sci. 6, 634 (2013).
10. S. Kment, Z. Hubicka, J. Krysa, D.Sekora, M. Zlamal, J. Olejnicek, R. Zboril. On the improvement of PEC activity of hematite thin films deposited by high-power pulsed magnetron sputtering method. Appl. Catalysis B:Env.165, 344 (2015).
11. L. Zhao, J. Xiao, H. Huang, Q. Huang, Y. Zhao, Y. Li. Enhanced efficiency of hematite photoanode for water splitting with the doping of Ge. Int. J. Hydrogen Energy. 43, 12646 (2018).
12. F. Wang, L. Song, H. Zhang, L. Luo, D. Wang, J. Tang. One-dimensional metal-oxide nanostructures for solar photocatalytic water-splitting. J. Electron. Mater. 46, 4716 (2017).
13. G. Rahman, O. S. Joo, S. Y. Chae, A. H. Shah, S. A. Mian. Enhanced water oxidation photoactivity of nano-architectured α-Fe_2O_3-WO_3 composite synthesized by single-step hydrothermal method. J. Electron. Mater. 47, 2359 (2018).

14. G. Kaura, Divya, S. A. Khan, V. R. Satsangi, S. Dass, R, Shrivastav. Nano-hetero-structured thin films, ZnO/Ag-(α) Fe_2O_3, with n/n junction, as efficient photoanode for renewable hydrogen generation via photoelectrochemical water splitting. Renew. Energy. 164, 156 (2021).
15. P. Liu, C. Wang, L. Wang, X. Wu, L. Zheng, H. G. Yang. Ultrathin hematite photoanode with gradient Ti doping. Research 2020, 5473217 (2020).
16. X. Wang, W. Gao, Z. Zhao, L. Zhao, J. P. Claverie, X. Zhang, J. Wang, H. Liua, Y. Sang. Efficient photo-electrochemical water splitting based on hematite nanorods doped with phosphorus. Appl. Catal. B-Environ. 248, 388 (2019).
17. C. Feng, S. Fu, W. Wang, Y. Zhang, Y. Bi. High-crystalline and high-aspect-ratio hematite nanotube photoanode for efficient solar water splitting. Appl. Catal. B-Environ. 257, 117900 (2019).
18. J. Deng, Q. Zhuo, X. Lv. Hierarchical TiO_2/Fe_2O_3 heterojunction photoanode for improved photoelectrochemical water oxidation. J. Electroanal. Chem., 835, 287 (2019).
19. D. Chen, Z. Liu, S. Zhang. Enhanced PEC performance of hematite photoanode coupled with bimetallic oxyhydroxide NiFeOOH through a simple electroless method. Appl. Catal. B: Environmental, 265, 118580 (2020).
20. A. A. Tahir, M. A. Mat- Teridi, K. U. Wijayanth. Photoelectrochemical properties of texture- controlled nanostructured α- Fe_2O_3 thin films prepared by AACVD. pss (RRL) 8, 976 (2014).
21. N. A. Arzaee, M. F. Noh, A. Ab Halim, M. A. Rahim, N. A. Mohamed, J. Safaei, A. Aadenan, S. N. Nasir, A. F. Ismail, M. A. Teridi. Cyclic voltammetry-A promising approach towards improving photoelectrochemical activity of hematite. Ceram. Int. 45, 16797 (2019).
22. G. S. Pawar, A. A. Tahir. Unbiased spontaneous solar fuel production using stable $LaFeO_3$ photoelectrode. Sci. Rep. 8, 1 (2018).
23. A. Martinez, J. Pena, M. Labeau, J. M. Gonzalez-Calbet, M. Vallet-Regi. The deposition of α–Fe_2O_3 by aerosol chemical vapor deposition. J. Mater. Res. 10,1307 (1995).
24. P. Scherrer. Estimation of the size and internal structure of colloidal particles by means of Röntgen rays. Göttinger Nachrichten Math. Phys. 2, 98 (1918).
25. H. S. Choi, S. W. Rhee. Effect of Carrier Gases on the Chemical Vapor Deposition of Tungsten from WF6-SiH_4. J. Electrochem. Soc. 141, 475 (1994).

673 26. D. Peeters, A. Sadlo, K. Lowjaga, O. Mendoza Reyes, L. Wang, A. Devi. Nanostructured Fe_2O_3 processing via
674 water- assisted ALD and low- Temperature CVD from a versatile iron ketoiminate precursor. Adv Mater.
675 Interfaces, 4, 1700155 (2017).
676 27. C. S. Enache, Y. Q. Liang, R. Van de Krol. Characterization of structured α-Fe_2O_3 photoanodes prepared via
677 electrodeposition and thermal oxidation of iron. Thin Solid Films 520, 1034 (2011).
678 28. J. A. Morales-Morales. Synthesis of hematite a-Fe_2O_3 nano powders by the controlled precipitation method.
679 Cienc en Desarro 8, 99 (2017).
680 29. M. Hanesch. Raman spectroscopy of iron oxides and (oxy) hydroxides at low laser power and possible
681 applications in environmental magnetic studies. Geophys. J. Int. 177, 941 (2009).
682 30. D. L. De Faria, S. Venâncio Silva, M. T. De Oliveira. Raman microspectroscopy of some iron oxides and
683 oxyhydroxides. J. Raman Spectrosc. 28, 873 (1997).
684 31. X. Su, C. Yu, C. Qiang. Synthesis of α-Fe_2O_3 nanobelts and nanoflakes by thermal oxidation and study to their
685 magnetic properties. Appl. Surf. Sci. 257, 9014 (2011).
686 32. S. H. Shim, T. S. Duff. Raman spectroscopy of Fe_2O_3 to 62 GPa. Am. Mineral. 87, 318 (2002).
687 33. S. S. Shinde, R. A. Bansode, C. H. Bhosale, K. Y. Rajpure. Physical properties of hematite α-Fe_2O_3 thin films:
688 J. Semicond 32, 013001 (2011).
689 34. S. Shen, S. A. Lindley, X. Chen. Hematite heterostructures for photoelectrochemical water splitting: rational
690 materials design and charge carrier dynamics. J. Z. Zhang, Energy Environ. Sci. 9, 2744 (2016).
691 35. D. A. Wheeler, G. Wang, Y. Ling, Y. Li, J. Z. Zhang. Nanostructured hematite: synthesis, characterization,
692 charge carrier dynamics, and photoelectrochemical properties. Energy Environ. Sci. 5, 6682 (2012).
693 36. Z. Zhang, I. Karimata, H. Nagashima, S. Muto, K. Ohara, K. Sugimoto, T. Tachikawa. Over 16% efficiency
694 organic photovoltaic cells enabled by a chlorinated acceptor with increased open-circuit voltages. Nat.
695 Commun. 10, 1 (2019).
696 37. R. Singaravelan, S. B. Alwar. Electrochemical synthesis, characterization, and phytogenic properties of silver
697 nanoparticles. Appl. Nanosci. 5, 983 (2015).
698 38. B. Abdullah, A. Ismail, H. Kashoua, W. Zetoun. Effects of deposition time on the morphology,
699 structure, and optical properties of PbS thin films prepared by chemical bath deposition.
700 Journal of Nanomaterials, 2018, 1826959 (2018).

39. M. Vanags, A. Sukta, J. Kleperis, P. Shipkovs. Comparison of the electrochemical properties of hematite thin films prepared by spray pyrolysis and electrodeposition. Ceram. Int., 41, 9024 (2015).
40. S. Shen, C. X. Kronawitter, D. A. Wheeler, P. Guo, S. A. Lindley, J. Jiang,S. S. Mao. Physical and photoelectrochemical characterization of Ti-doped hematite photoanodes prepared by solution growth. J. Mater. Chemistry A, 1, 14498 (2013).
41. L. P. de Souza, R.O.G. Chaves, A. Malachias, R. Paniago, S.O. Ferreira, A.S. Ferlauto. Influence of annealing temperature and Sn doping on the optical properties of hematite thin films determined by spectroscopic ellipsometry. J. Appl. Phys. 119, 245104 (2016).
42. K. Sivula, R. Zboril, F. Le Formal, R. Robert, A. Weidenkaff, J. Tucek, J. Frydrych, M. Gratzel. Photoelectrochemical water splitting with mesoporous hematite prepared by a solution-based colloidal approach. J. Am. Chem. Soc. 132, 7436 (2010).
43. E. S. Cho, M. J. Kanga, Y.S. Kang. Enhanced photocurrent density of hematite thin films on FTO substrates: effect of post-annealing temperature. Phys. Chem. Chem. Phys.17, 16145 (2015).
44. K. L. Foo, M. Kashif, U. Hashim, W. W. Liu. Effect of different solvents on the structural and optical properties of zinc oxide thin films for optoelectronic applications. Ceram. Int. 40, 753 (2014).
45. S. Hernández, G. Barbero, G. Saracco, A. L. Alexe-Ionescu. Considerations on oxygen bubble formation and evolution on $BiVO_4$ porous anodes used in water splitting photoelectrochemical cells. J. Phys. Chem. C. 119, 9916 (2015).
46. T. Lopes, L. Andrade, F. Le Formal, M. Gratzel, K. Sivula, A. Mendes. Hematite photoelectrodes for water splitting: evaluation of the role of film thickness by impedance spectroscopy. Phys. Chem. Chem. Phys. 16, 16515 (2014).
47. P. S. Bassi, L. Xianglin, Y. Fang, J. S. Loo, J. Barber, L. H. Wong. Understanding charge transport in non-doped pristine and surface passivated hematite (Fe_2O_3) nanorods under front and backside illumination in the context of light induced water splitting. Phys. Chem. Chem. Phys. 18, 30370 (2016).
48. T. Lopes, L. Andrade, H. A. Ribeiro, A. Mende. Characterization of photoelectrochemical cells for water splitting by electrochemical impedance spectroscopy. Int. J. Hydrogen Energy. 35, 11601 (2010).
49. A. Boudjemaa, S. Boumaza, M. Trari, R. Bouarab, A. Bouguelia. Physical and photo-electrochemical characterizations of α-Fe_2O_3. Application for hydrogen production. Int. J. Hydrogen Energy. 34, 4268 (2009).

50. L. Xi, C. Schwanke, D. Zhou, D. Drevon, R. van de Krol, K. M. Lange. In situ XAS study of CoB i modified hematite photoanodes. Dalton Trans. 46, 15719 (2017).
51. A. Aruchamy, G. Aravamudan, G. S. Rao. Semiconductor based photoelectrochemical cells for solar energy conversion-an overview. B. Mater. Sci. 4, 483 (1982).
52. Y. Lin, G. Yuan, S. Sheehan, S. Zhou, D. Wang, Hematite-Based Solar Water Splitting: Challenges and Opportunities. Energy Environ. Sci. 4, 4862 (2011).
53. A. Subramanian, M. A. Mahadik, J.W. Park, I. K. Jeong, H. S. Chung, H. H. Lee, S. H. Choi, W. S. Chae, J. S. Jang. An effective strategy to promote hematite photoanode at low voltage bias via Zr^{4+}/Al^{3+} co-doping and CoOx OER co-catalyst. Electrochim. Acta 319, 444 (2019).

Figure Captions:

Fig.1. Representative PXD patterns from films prepared by using $FeCl_3$ precursor in methanol annealed at 525° C by; (a) CVD and SP method with standard JCPDS card # 00-024-0072 (b) AACVD method at different processing temperatures.

Fig. 2. Raman spectra of hematite thin films in (a) ethanol and (b) in methanol at 450-525°C for 30 minutes deposition time by AACVD at different temperatures.

Fig. 3. SEM images of hematite thin films prepared at 525°C from $FeCl_3$ by (a) SP (b) CVD and (c) AACVD methods; (d) cross sectional image of the film prepared by AACVD method.

Fig. 4. (a) Absorbance spectra of iron oxide films prepared from $FeCl_3$ in methanol at different temperatures for 30 minutes by the AACVD method; (b) Tauc plots taken from the absorption spectral data; (c) Kubelka – Munk plots using absorption data for the calculation of sample band gaps.

Fig. 5. LSVs, in 0.1M NaOH at $10mVs^{-1}$, in darkness, under illumination and in chopped light for the α-hematite films prepared by spray pyrolysis at 525°C using three different precursors: (a & b) in ethanol and (c & d) in methanol solvent .

Fig. 6. LSVs, in 0.1M NaOH at $10mVs^{-1}$, for iron oxide thin films fabricated by CVD using $FeCl_3$ in (a & b) ethanol and (c &d) in methanol at 500 °C for different film deposition times. LSVs conducted in darkness and under illumination (a,c) and under chopped light (b,d) are shown.

Fig. 7. LSVs, in 0.1M NaOH at $10mVs^{-1}$, for hematite thin films fabricated at 525 °C by the AACVD method using $FeCl_3$ and (a & b) ethanol or (c &d) methanol for different film deposition times. LSVs are taken in darkness and under full illumination in (a, c) and under chopped light in (b, d), comparative photocurrent stability plots of AACVD films fabricated from $FeCl_3$ at 525°C using methanol and ethanol with 30 min deposition time (e).

Fig. 8 EIS analysis of optimized hematite thin films prepared by AACVD using methanol at 525°C (a) Nyquist plots (b) Bode plots. (c) Plot of evolved hydrogen and oxygen as a function of time over 6 h, using an optimized hematite electrode in aqueous 0.1 M NaOH.

Improved Photoelectrochemical Performance of Chemically Grown Pristine Hematite Thin Films

Saima Qureshi[a,b,] Duncan H. Gregory[b], Asif Ali Tahir [c], Safeer Ahmed[a,] *

Department of Chemistry, Quaid-i-Azam University, 45320, Islamabad, Pakistan.

WestCHEM, School of Chemistry, University of Glasgow, Glasgow G12 8QQ, United Kingdom.

Environment and Sustainability Institute (ESI), University of Exeter, Penryn Campus, TR10 9FE, United Kingdom.

*Corresponding author's e-mail addresses: safeerad@qau.edu.pk

Tel: 00-92-51-90642145, Fax: 00-92-51-90642241

Abstract

The alpha phase of hematite (α-Fe_2O_3) is one of the most promising catalysts for photoelectrochemical (PEC) water splitting amongst several photoanode materials due to its suitable bandgap and stability in aqueous solutions. The surface structure and morphology of films play pivotal roles in the enhancement of water oxidation reaction kinetics. In this work, α-Fe_2O_3 films were produced via either spray pyrolysis (SP), chemical vapor deposition (CVD) or aerosol-assisted chemical vapor deposition (AACVD). Their structural and morphological properties were subsequently characterized by powder X-ray diffraction (PXD), scanning electron microscopy (SEM) and Raman spectroscopy. High quality thin films were best achieved by AACVD annealed at 525°C, possessing an average thickness of 0.75µm with 85% transmittance and an optical absorption onset at 650 nm. The results evidently showed that the thermal oxidation process achieved at 525°C eliminated undesired impurity phases such as FeO and Fe_3O_4 and enabled the microstructure to be optimized to facilitate the generation and transport of photogenerated charge carriers. The optimized α-Fe_2O_3 film showed a stable PEC water oxidation current density of ~1.23 mA cm^{-2} at 1.23 V (vs. RHE), with an onset potential of 0.76 V, under AM 1.5 irradiation. The obtained higher current density of pristine α-Fe_2O_3 thin films obtained by AACVD method is unique and the films presented good photocurrent stability with 92% retention after 6 h. Data form electrochemical impedance spectroscopy (EIS) corroborated these results, identifying fast charge transfer kinetics with decreased resistance and an electron lifetime of 175 µs. Quantitative measurements showed that 1.2 µmol cm^{-2} of oxygen could be produced at the photoanode in 6 h.

Key words: hematite; photocurrent; hydrogen generation; electrochemical impedance; electron lifetime; AACVD.

Graphical Abstract

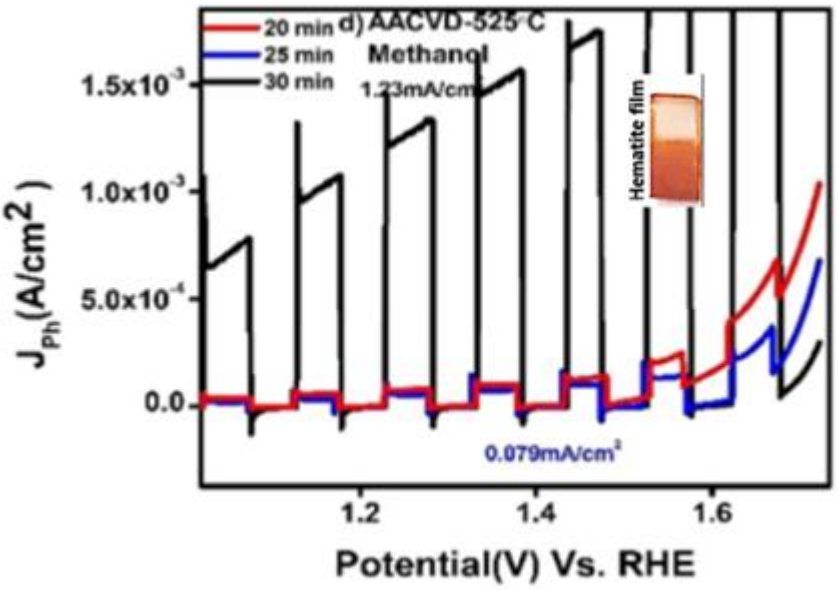

1. Introduction

The photoelectrochemical (PEC) generation of hydrogen is one of the most promising ways to make the best use of renewable solar energy. In a PEC cell, water molecules are broken into hydrogen and oxygen gases on the surfaces of the photocathode and photoanode, respectively. For a material to act as a photocatalyst in a PEC cell, it needs a suitable band gap in the range of 1.23 to 1.6 eV [1]. Further, the valance and conduction band edges should be compatible with the standard electrode potentials of hydrogen gas and oxygen gas evolution. More specifically for the water reduction reaction (H^+/H_2), the conduction band edge of the material needs to be at a potential less than (more negative than) 0 V vs. normal hydrogen electrode (NHE) while the valence band needs to be at a potential higher than (more positive than) 1.23 V vs. NHE for water oxidation (H_2O/O_2). This demands the material must have a light absorption onset at or slightly below 1008 nm [2].

It is well recognized that photocatalysts which utilize ultraviolet (UV) light for hydrogen production via solar water splitting perform better than those which utilize only the visible part of the spectrum due to the higher energy photons

that exist in the former case. On the other hand, the relative proportions of UV (<400 nm), visible (400–800 nm) and infrared (>800 nm) light in the solar spectrum are 4%, 53% and 43%, respectively. Therefore, it is critical to design a photocatalyst which can combine both a high absorption coefficient with a wide absorption window. Consequently, a relatively low-efficiency photocatalyst that is able to absorb a significant portion of visible light can be more useful than a higher-efficiency photocatalyst that absorbs solely in the ultraviolet regime.

Among potentially suitable oxide semiconductor materials such as TiO_2 (with a band gap, E_g, of 3.2 eV), ZnO (E_g = 3.1 eV), and WO_3 (E_g = 2.7 eV), hematite, α-Fe_2O_3 (E_g = 2.1 eV) is considered most promising for PEC water splitting given that it can absorb a major portion of visible light; it possesses excellent stability under alkaline conditions and that it is environmentally benign, earth-abundant (constituting 6.3% of the Earth's crust) and of low cost [3]. The relatively small band gap compared to its oxide competitors, enables it to harvest around 40% of the solar spectrum (up to ~600 nm wavelength). Although, hematite has a theoretical solar-to-hydrogen (STH) efficiency of 14-15%, which is very impressive [4], however, the reported experimental efficiencies for hematite photoanodes are significantly lower. This disparity is mainly due to the short hole diffusion length (2-4 nm) when compared with the single-path optical absorption length or maximum light penetration depth of 118 nm in hematite at a wavelength of 550 nm [4]. Consequently, one can consider only the holes which are produced in the proximity of the hematite/electrolyte interface to participate in water oxidation and generate the photocurrent. Conversely, the holes generated further away from the hematite/electrolyte interface are lost to charge recombination processes. Therefore, the challenge lies in improving the charge carrier diffusion length and maximizing the optical absorption depth while maintaining an appropriate film thickness.

To overcome such limitations, several strategies have been developed to improve the PEC properties of α-Fe_2O_3 such as by modifying the electronic structure via elemental doping [1,3], by synthesizing nanostructured α-Fe_2O_3) [3,4], by integrating α-Fe_2O_3-based composite photoanode with better conducting materials [1,3], or by decorating the surface of α-Fe_2O_3 with a co-catalyst [1,3] to facilitate the oxygen evolution reaction (OER). Compared to the hydrogen evolution reaction (HER) at the photocathode (which is usually platinum), the four-electron transfer OER at the photoanode is the rate-limiting step in the overall process. Although hematite has an appropriate valence band edge (2.4 to 2.7 eV) for the OER in water oxidation, the conduction band minima (0.3 to 0.6 eV) is lower than the required value for the hydrogen evolution reaction (HER) [4]. Consequently, the development of a high efficiency photoanode is the critical step in designing improved devices.

The US Department of Energy recommends that a PEC device should cost less than US$ 160 per m^2 with a solar-to hydrogen (STH) efficiency of approximately 10% [3] (which is below the maximum theoretical efficiency of 15% calculated for many metal oxide photoanodes). [3]. The maximum theoretical STH efficiency of hematite is *ca*. 15% and substantially higher than the STH benchmark efficiency of 10% required for commercial applications [1,4-7]. However, to achieve such an efficiency practically, hematite needs to overcome issues such as low electrical conductivity, slow charge transfer kinetics at the electrode/electrolyte interface and a high overpotential. Since 1978 substantial research has been performed to understand the basis of these issues and to improve PEC performance as a result. The highest photocurrent density (J_{Ph}) reported for a pristine hematite photoanode was 1.26 mA cm^{-2} in 2013 [7]. The report describes a single-crystalline "wormlike" hematite film prepared on fluorine doped tin oxide (FTO) by first forming 1-D β-FeOOH nanorods and then converting them to α-Fe_2O_3 by a two-step annealing treatment at relatively higher temperatures of 500 and 800°C. The measured photocurrent is then further improved by the addition of oxygen evolution cocatalysts (Co-Pi) to modify the surface properties. The resulting hematite photoanode showed a PEC water oxidation current of 4.32 mA cm^{-2} at 1.23 V vs. RHE under simulated 1-sun (100 mW cm^{-2}) irradiation. The system could produce 555 µmol cm^{-2} of H_2 in 3 h.

The most recent reports of high J_{pj} values are those in which hematite is modified either by doping or through surface treatments [7-14]. Zhao et al. [11] used Ge as a dopant to obtain modified hematite films with a current density of 0.92 mA cm^{-2} while Zandi *et al* [9] adopted a strategy of titanium doping to improve the charge transfer characteristics of bulk hematite to yield 2.8 mA cm^{-2} at 1.23 V vs RHE. More recently, Liu *et al*. also added Ti, synthesizing doped ultrathin hematite photoanodes via a layer-by-layer polymer assisted deposition method to record a photoanode current density of 1.30 mA cm^{-2} [15]. Employing co-catalyst, nano-structuring and non-metallic doping approaches have also been adopted such as phosphorous doping considerably increased the current density upto 2.0mAcm^{-2}[14,16] and the decoration of hematite films with a FeOOH/NiOOH as dual cocatalyst also caused an improvement in the current density [17]. In a report in 2018, one-step in-situ synthesis of hematite–tungsten oxide (α-Fe_2O_3–WO_3) composite on fluorine-doped tin oxide (FTO) substrate was carried out via simple hydrothermal method. The obtained electrode could demonstrate water oxidation photocurrent density of just 0.80 mA/cm^2 (at 1.6 V vs. reversible hydrogen electrode under standard illumination conditions [13]. As the interfacial sites affect the properties of the photocatalyst therefore, interfacial layering of the hematite with different dopants and blends have been exploited for improved efficiency in recent years [18-19]. Processing routes have also become important in mediating film quality and

performance as with slight variations in structure or morphology often strongly influencing the light absorption and charge transport properties of the material. Aerosol-assisted chemical vapour deposition (AACVD) has proven to be very successful in producing high performance films. Tahir *et al* originally demonstrated the potential of this method, producing a hematite film with a photocurrent density of 455µA cm^{-2} at 1.23 V vs RHE [20]. Subsequently a current density of 585 µAcm^{-2} at 1.23 V vs. RHE was obtained in a hematite film by using AACVD method. [21].

In present work, we assessed the importance of processing techniques by synthesizing nanostructured α-Fe_2O_3 thin films via three different methods, namely: spray pyrolysis (SP), chemical vapor deposition (CVD), and AACVD. The thin films were fabricated into photoanodes on conducting glass substrates for structural and morphological characterization and for extensive, optical, electrochemical and photoelectrochemical testing. Systematic investigation of the effects of Fe^{3+} precursors, annealing temperature and solvent on film structure and quality enabled us to determine the optimum conditions for each processing method. The aim of the study was to develop pristine α-Fe_2O_3 photoanodes with improved surface properties so as to maximize the diffusion lengths of the PEC-generated charge carriers and enable fast carrier transport. The results showed that the AACVD method, in particular, can be employed to produce the quality thin films, which are evenly structured, with sufficiently large surface area, and which could reduce recombination rate and increase carrier diffusion lengths [22]. In this way, a substantial photocurrent density of 1.23 mA cm^{-2} could be achieved for pristine hematite without any doping or surface treatment through AACVD just at 525°C temperature. The hydrogen gas evolution reaction was indirectly monitored, and the yield of the gas was quantified.

2. Experimental

2.1 Materials Used

Iron acetylacetonate $(C_5H_8O_2)_3Fe$ (99.9%), ferric chloride 99% and ferric nitrate nonahydrate 99% (Aldrich), absolute methanol (Fisher Scientific) and ethanol (Alfa Aeser) were obtained commercially and used without further purification. Fluorine-doped tin oxide (FTO) (TEC 8 Pilkington, 8 Ω/square) was used as conducting glass substrate. Doubly de-ionized water (DDW), (MilliQ water, from Elga system) with a resistivity of *ca.* 18.2 M Ω cm was used for the preparation of solutions.

2.2 Procedures and methodology

Three methods namely, spray pyrolysis (SP), chemical vapour deposition (CVD), and aerosol assisted chemical vapour deposition (AACVD) were used for the thin film preparation. Texture-controlled nanostructured hematite thin films were fabricated by using iron (III) chloride as the precursor in either ethanol or methanol. The FTO glass substrates were cleaned ultrasonically prior to use for thin film preparations using ethanol, iso-propanol and acetone for 15 minutes each, in sequence, and then washed with de-ionized water to remove any remaining impurity before drying with compressed air.

2.2.1 Spray pyrolysis

The spray pyrolysis setup comprised of a syringe pump system (New Era Pump System NE-1000), an ultrasonic atomizer nozzle (Sonozap) 1 mm diameter and a vortex attachment. The cleaned FTO glass substrate was set on the hot plate at 150 °C so as to maximise the coverage from the syringe pump. Compressed air was passed through a vortex attachment at 4 L min^{-1} to generate a large plume of aerosol in order to achieve a uniform coverage of the FTO. The Fe_2O_3 photoelectrodes were prepared by spraying 5 ml each of methanolic and ethanolic precursor solutions of 0.1 M $FeCl_3$, $Fe(NO_3)_3 \cdot 9H_2O$ and $Fe(acac)_3$, respectively at 150 °C for 20, 25 and 30 minutes on to the FTO at a rate of 0.60 ml min^{-1} for 40 minutes. The resultant films (**Fig. S1)** were heated at different temperatures, 450 °C, 475°C, 500°C and 525 °C with a ramp rate of 25 °C h^{-1} to produce single phase, crystalline Fe_2O_3 material. The complete description of iron oxide thin films prepared by using different solvents, precursors and for different deposition times and temperatures is given in **Table SI**.

2.2.2 Chemical vapor deposition

In a typical CVD experiment, 20 ml of 0.1 M solution of $FeCl_3$ in ethanol was combined with 0.1 ml of acetylacetonate in a 50 ml round-bottom flask. An FTO substrate was placed in a tube furnace for each deposition experiment and air was used a carrier gas, at a flow rate of 130 ml min^{-1}. Different deposition temperatures between 450, 475 and 500 °C were employed across a series of experiments. Films were deposited from precursor solution for time periods of 10,15,20,25 and 30 min at fixed temperatures. The deposition temperature and time were monitored and programmed to control the morphology of the thin films. At least five films were fabricated for a given deposition time at each set temperature. A comprehensive information of variables is given in **Table SII**.

2.2.3 Aerosol assisted chemical vapor deposition

Nanostructured α- Fe_2O_3 thin films were deposited on FTO glass substrate by AACVD using $FeCl_3$ as precursor. The 0.1 M methanolic and ethanolic precursor solutions were each used to generate aerosols. Each aerosol was generated by means of a pneumatic collision generation method, using a TSI Model 3076 constant output atomizer, which typically generates 0.3 μm-sized aerosol droplets. A stream of compressed air running at 2 bar constant pressure during depositions was used to transfer the aerosol to the reaction chamber. Air was used as a carrier gas, at a flow rate of 150 ml min^{-1} and deposition temperatures between 450 °C and 525 °C were employed (in 25°C increments using a hot plate). Each film was deposited for a period of 20, 25 and 30 min. In addition to the hotplate thermometer, the temperature of the FTO substrate surface was also measured using an additional external thermocouple taking readings prior to and during deposition. The experimental details are given in **Table SIII** and the films produced are shown in **Fig. S1**.

2.3. Instrumentation and characterization techniques

An X'Pert PRO MPD diffractometer equipped with a monochromator, employing Cu Kalpha1 radiation was used to analyze the phase purity and crystallinity of the deposited films by powder X-ray diffraction (PXD). Diffraction data were collected in from 5.0027 to 84.9617 (minimum step size $2\theta = 0.001°$). Raman spectroscopy was performed with a Horiba LabRAM HR Raman microscope equipped with a Helium Cadmium IK3201R-F UV Laser (325 nm; 20mW) and a Ventus 532 visible laser (532 nm; 200 mW). All samples were run with 50x objective. Scanning electron microscopy (SEM) coupled with energy dispersive X-ray spectroscopy (EDX) was performed to assess the morphology and the elemental composition of the Fe_2O_3 nanocrystalline films. A MIRA 3 TESCAN instrument with SEM magnification 25.0kx and SEM HV 20.0kv,BI 9:00 are used for these experiments.

For optical characterization, a PerkinElmer lambda 1050 spectrophotometer equipped with a 150 mm InGaAs sphere was used to record diffuse reflectance and absorbance UV-visible spectra. Electrochemical, EIS and photoelectrochemical measurements were conducted using a typical three electrode set-up fitted with a quartz window. The electrode configuration comprised of various α-Fe_2O_3 thin film samples deposited on FTO as a working electrode, Ag/AgCl/3M KCl as a reference electrode and Pt wire as a counter electrode immersed in 0.1 M NaOH electrolyte (pH ~ 13). The measurements were made with a micro-Autolab, type III potentiostat/galvanostat set-up. An AM1.5

class-A solar simulator (Solar Light 16S-300) was used as an illumination source in photoelectrochemistry experiments. The electrode was illuminated through the electrolyte side utilizing an illumination area of 1 cm^2 and measurements were made at a scan rate of 0.01 Vs^{-1} scan rate both in darkness and in chopped light.

Gas chromatography (GC) measurements were made as described previously [23] and reproduced as such. "A manual injection GC system (PerkinElmer Clarus 580) using a molecular sieve (PerkinElmer) and a pulsed discharge detector (PDD) with an argon flow of 28 ml/min were used. A custom-made glass reactor vessel with an attached fused silica viewport containing 0.1 M NaOH (pH 13) with a dead space of 100 ml was purged with argon for 2 hours with gentle heating and stirring to remove atmospheric air from the system. No sacrificial agents were used. The sealed vessel contained the working Fe_2O_3 electrode connected to a Pt mesh by a single outer wire and was subjected to light illumination for the water splitting reaction. GC measurements were carried at an interval of 1 hour [23]".

3. Results and Discussions

3.1 Structural and morphological characterization

3.1.1 PXD analysis:

PXD analysis was performed on each of the film samples synthesized by SP, CVD and AACVD methods, primarily to ascertain phase purity of the anticipated α- Fe_2O_3 samples. The representative results are shown in **Fig.1** while others in **Fig. S2,** and **Table SIV**. It is apparent from peak pattern of all the α- Fe_2O_3 films, deposited by three methods on FTO substrate, that apart from dense SnO_2 diffraction peaks due to FTO at least three characteristic peaks of hematite, specifically (104), (110) and (300) are visibly present. In addition to these reflections some weaker peaks corresponding to the (012), (006), (113), (024), (116), and (122) planes are also observable. All the observed reflections are closely matched with the standard values (JCPDS-00-024-0072) of the inter-planar distance *d* for hematite [21] and are indexed to their respective Miller indices. The absence of some of the peaks may be due to very intense peaks of the substrate and slight 2θ shift for some of the peaks could be ascribed to the lattice mismatch between substrate and film which causes strain in the film lattice.

Among the films prepared via the three different synthesis methods, those produce by CVD most closely resemble the standard hematite diffractograms in terms of number of characteristic peaks and intensities **(Fig.S2**). The apparent slight mismatches in the line pattern are artifacts occurred while grouping all patterns in one figure. The PXD patterns

obtained were converted into line patterns because the peaks of α-Fe_2O_3 were suppressed by the reflections due to FTO substrate. The original PXD patterns of the films prepared from the three methods and by AACVD method at different temperatures are shown in **Fig.1.** The PXD patterns of the films prepared under different experimental conditions are available in supplementary data **(Fig.S2). Fig.1a,** represents PXD patterns of α-Fe_2O_3 formed by three methods at optimized conditions, wrt PEC performance (discussed alter), of precursor ($FeCl_3$), solvent, temperature, and deposition time.

Fig.1.

The PXD data for the films deposited at different temperatures are normalized to the high intensity FTO peak at 37.9°. Martínez et al. [24] reported the deposition of α-Fe_2O_3 films and found that structural properties such as crystallinity and phase purity are strongly dependent on the deposition temperature. The current analysis proved the same and appearance of no other iron oxide phase in the PXD patterns in **Fig.1** is suggesting the suitability of the procedures adopted for the preparations of pure α-Fe_2O_3 thin films using $FeCl_3$ precursor. The crystallite diameter (*B*) was approximated according to Scherrer's formula [25], as given below in equation 1, and the measured and calculated results are collated in **Table SIV**.

$$B\ (2\theta) = K\lambda / \beta \cos\theta \qquad \textbf{(1)}$$

where β is the full width at half maximum (FWHM) of each diffraction peak. A Scherrer constant of K = 0.9 was employed, consistent with a rhombohedral crystal system. Cu-Kα radiation was used throughout, with wavelength, λ = 1.5406 Å,.

Films obtained by the SP method gave crystallite diameters varying from approximately 5-20 nm for the corresponding temperature range of 450 ºC,475 ºC,500 ºC and 525 ºC in ethanol solutions, i.e., with a decrease in particle size on increasing annealing temperature. On changing the spray solvent to methanol, the crystallite size varied from approximately 3-23 nm over the same temperature range. However, in methanol solvent the variation in crystallite size was same in comparison to AACVD method. The film composition, surface morphology, deposition rate, and the internal structure are dependent on the momentum and thermal diffusivity of the carrier gas and as a result the mean free path and mass diffusivity of the reactant molecules are also affected on changing the carrier gas. It is observed in

other works that high thermal diffusivity and high molecular velocity of helium gas lowers the deposition rate due to the formations of intermediate species which can go out of the reactor [26], but this is not important here. The effect of precursor solutions was also investigated by SP method. It was found that the films prepared using Fe(accac) gave consistently smaller crystallite diameters (average values ranging 5 – 8 nm) in comparison to the sizes calculated for the films obtained from $FeCl_3$ and $Fe(NO_3)_3.9H_2O$ precursors.

A similar trend of decreasing crystallite size, with increasing temperature (425 to 525 ^oC) was also observed for films prepared by the CVD method. In this case, crystallites varying from approximately 5-23 nm were produced. For employing iron oxide as photoanode in photoelectrochemical water splitting a crystalline, nanostructured deposit is desirable [27-28]. As expected, the deposition temperature has a significant impact on the crystallinity of the films. Increasing the temperature to 600, 700, and 800 °C leads to additional and more intense reflections. Due to the low intensity of the reflections in the XRD patterns, it is difficult to assign the structures. The morphological appearance of the iron oxide deposits, beside its crystallinity, is of high impact considering the performance of the material in photoelectrochemical (PEC) water splitting. This means the CVD-grown Fe_2O_3 films essentially behave as conventional compact n-type semiconductors in which the efficiency-limiting factor is the short diffusion length of the minority charge carriers (holes).

Of the thin films prepared by the three different techniques employed, those fabricated by the AACVD method yielded diffraction patterns with the strongest resemblance to that hematite (ICDD PDF 00-24-0072), with characteristic peaks corresponding to the (012),(104),(110),(116),(214) and (300), reflections (**Fig. 1**). The sharp and intense peaks indicate the presence of pure crystalline alpha phase hematite (α-Fe_2O_3). The calculated crystallite size is in the range of 6 to 7nm. In the films by AACVD method the higher intensity of the (104) and (110) peaks indicate that the α-Fe_2O_3 particles are orientated in the said directions. For water splitting application it is a favorable result because the conductivity of α-Fe_2O_3 along the (110) direction is higher than that in the orthogonal direction [27- 28]. Most of the peaks correspond to Fe_2O_3 are indexed to rhombohedral system (JCPDS 00-024-0072). The intensity of the peaks increases with temperature and the peak at (214) is shifted towards left i.e., lower 2θ value whilst the rest of the peaks are shifted slightly towards higher 2θ values in comparison to reference hematite. The peaks for 475°C sample are diminished, therefore the FTO peaks are also not apparent.

Comparing among the three preparation methods it is apparent that the crystallite size of the films obtained from the AACVD method is smallest and provides the least variation on changing the film processing temperature. The observed change in morphology with the increase in temperature is attributed to the gradual shift of nucleation from heterogeneous to homogeneous process. The mechanism of AACVD deposition and the effect of homogeneous or heterogeneous nucleation on the texture and morphology of thin films has been discussed in detail elsewhere [20] The PXD patterns of the full set of films prepared by the three methods at 475 °C and 500 °C are shown in **Fig S2**.

3.1.2 Raman analysis:

A typical Raman spectrum of a α-Fe_2O_3 film consists of clearly visible bands at 225, 245, 291, 411, 500, 611 and 1321 cm^{-1}[29]. Hematite crystallizes in the D^6_{3d} space group and seven bands are expected in the Raman spectrum. As shown elsewhere, the Raman spectrum of an α-Fe_2O_3 film on FTO substrate is dominated by two A_{1g} modes at 225 cm^{-1} and 500 cm^{-1}, and three E_g modes at 299.7 cm^{-1}, 399.8 cm^{-1} and 607.6 cm^{-1} [30]. Additionally, FTO substrate bands can also appear in experimental spectra. In many cases, it is reported that a band at *ca*. 245 cm^{-1} is visible on the flank of the 225 cm^{-1} peak [30]. From the literature, a further band at approximately 1305.7 cm^{-1}, can also be observed, which is associated with a vibration of unclear origin [29]. De-Faria et al. [31] suggest that this band is caused by the scattering of two magnons in the structure, but according to Su et al. [32], the band is a second harmonic vibration.

Fig. S3 compares the Raman spectra of α-Fe_2O_3 thin films on FTO after annealing at different temperatures for 30 min in ethanol, as prepared by all the three methods. The characteristic two A_{1g} (222 and 498 cm^{-1}) and five E_g (225 cm^{-1}, 243 cm^{1}, 290 cm^{-1}, 408 $cm^{-1}$and 608 cm^{-1}) bands are clearly visible in all the spectra. Considering first the results obtained for the CVD films, the experimental spectra are very much consistent with those reported for α-Fe_2O_3 across the measured Raman shift range. All the expected hematite bands are present, albeit broadened in comparison to the others reported previously [31]. In most cases, the 225 cm^{-1} band in the experimental spectra is flanked by the 245 cm^{-1} band.

The Raman spectra of hematite films prepared by SP methods also showed the characteristic seven bands across the measured Raman shift range: specifically the two A_{1g} modes (226 cm^{-1} and 497 cm^{-1}) and the five E_g modes (245 cm^{1}, 292 cm^{-1}, 298 cm^{-1}, 412 cm^{-1} and 613 cm^{-1}). The position of the peaks is in good agreement with literature data. Among

the three precursors used in the SP experiments, $FeCl_3$, $Fe(NO_3)_3.9H_2O$ and Fe(acac), the distinct sharp peaks with different intensities were of the films from the $FeCl_3$ [30] .

The Raman spectra of α-Fe_2O_3 prepared by AACVD at different temperatures in ethanol and methanol respectively for 30 minutes deposition time are shown in **Fig. 2a &b.** The respective spectra demonstrate all the characteristic peaks expected for α-Fe_2O_3, with the two A_{1g} mode bands at 224 cm^{-1} and 495 $cm^{-1}$and three E_g mode bands at 189 cm^{-1}, 289 cm^{-1}, and 412 cm^{-1}. Besides the typical A_{1g} and E_g symmetry phonon modes (below 620 cm^{-1}), a very strong feature was also detected at 1315 cm^{-1} when the spectral range was extended to 1500 cm^{-1}, which as discussed above, could be attributed to a second order phonon-photon interaction, [33]. In ethanol peaks at 475C are more prominent than at other temperatures, however, in methanol there is not much change in spectra for films annealed at various temperatures. A sudden jump below 500cm^{-1} for ethanol-based films could not be ascertained.

Fig. 2.

3.1.3 SEM analysis

The SEM images of the SP hematite films prepared at 525 °C are presented in **Fig. 3(a)**. From the images it is apparent that the surface of the films prepared by the SP method is composed of dense, irregular, and uneven pattern of agglomerates/clusters of different sizes ranging from 90 - 550 nm and an average particle size of 180 nm which is in good agreement with the SEM images reported in the literature [34-35]. The SEM images also show that the sintered microparticles are effectively non-porous.

A representative SEM image of a film prepared by the CVD method at a temperature of 525 °C is shown in **Fig3b**. The film has a very distinct morphology with sub-micron sized platelets clearly visible. These platelets are of sizes ranging between 0.5 to 1 µm in length, 100 to 150 nm in width and less than 50 nm in thickness. The coverage of the film surface is homogenous with an approximately uniform distribution over the entire surface. Each of the platelets appears to be smooth. The CVD-deposited films exhibit a higher internal surface area in comparison to those prepared by the SP method owing to have smaller particles.

Fig.3(c) shows the SEM image of hematite thin films deposited for 30 mins at 525°C using $FeCl_3$ in methanol via AACVD. The particle morphology is very similar to that obtained by CVD but with platelets of a much smaller size

(i.e., of length 250 - 300 nm). The width of the flakes is also in the nano-range (i.e., 60 – 100 nm), while the thickness is approximately 20 – 30 nm; about half that the platelets obtained by the CVD method. As the SEM image for the AACVD thin films is a bit blur therefore, the thickness of the platelets is a projected value based upon the length and width values. This in analogous to CVD results. From the variation in the dimensions of the particles it is speculated that the nanoparticles cluster up, however this needs further investigation and could be an interesting study. **Fig.3(d)** gives an estimate about the thickness of the film through cross sectional image.

All the α-Fe_2O_3 films adhered well to the FTO substrate regardless of preparation method and in each case the thickness of the film (typically from 0.475 to 0.91µm) showed a linear dependence with the deposition time. The films prepared by SP, CVD and AACVD, using methanol solvent and annealed at 525^{o}C, showed an average thickness of 0.745 µm, 0.91 µm and 0.475 µm thickness, respectively. The effect of the shape and size of the component particles is discussed with respect to the PEC performance of the films in later sections.

Fig. 3.

The EDX spectra taken of all the films confirm that there are no other elemental impurities in the prepared films and the theoretical and experimental ratios of the constituent elements (2:3 Fe:O) complement each other (**Fig. S4** shows each of the EDX spectra of the films in sequence). In view of the structural and morphological studies of the films prepared by three methods it was recognized that the films prepared by AACVD method are best and hence used for further property characterization studies.

Here the deposition time is affecting the thickness of the film which then affects crystalline structure, band gap, and absorption intensity of the films. To observe the effect of temperature on the XRD patterns of the films developed from three different methods, i.e., SP, CVD and AACVD, the deposition time was kept constant, and temperature was varied. The obtained results, **Table SIV**, clearly show that the crystallite size is found to decrease with the increase in temperature for SP and CVD methods but for AACVD it remains same. Grain size of the films by SP and AACVD at 525°C, given in **Fig.3**, is in nanoscale range, and the cross-sectional image of the film formed by AACVD (**Fig.3d**) indicates it is thinnest (0.475µm), though the thickness of films by other two methods is also less than 1 micrometer.

Referring to **Table SVI,** it is obvious that change in Eg is not following a much regular pattern with the change in temperature probably due to partial structural variation.

3.2 Optical and electrochemical characterization

3.2.1. Optical analysis -UV- Visible spectroscopy

The optical analysis was conducted on hematite thin films prepared by the AACVD method. **Fig. 4a** shows the absorption spectra of hematite thin films prepared by using $FeCl_3$ and methanol as solvent for 30 minutes at different temperatures. It is apparent that the absorption is negligible above 650 nm and as the wavelength continues to decrease, there is a marked increase in absorbance, which reaches its maximum value at approximately 530 nm. The artifact observed at 380 nm is due to a change of the light source in the spectrophotometer. Increasing the preparation temperature of the films does not result in any significant shifts in the position of the maxima or other features. Otherwise, the spectra are consistent with those previously reported for pure hematite films on an FTO substrate [34-35]. Considering the films prepared by the AACVD method at 550°C in methanol, an λ_{max} value of 540 nm is observed and the corresponding value of the absorption coefficient (α) can be calculated by using the measured film thickness of 0.475 µm) (as obtained from cross sectional SEM imaging) and by applying the following formula [34]:

$$\alpha = 2.303\,(A/d) \qquad \textbf{(2)}$$

Where *A* is the absorbance, 0.473 at 540nm, and *d* is the diffusion length. This yields of value of the absorption coefficient, $\alpha = 2.293 \mu m^{-1}$.

It has been reported that the lifetimes (of a few ps) and diffusion lengths (of *ca*. 2–4 nm) of the charge carriers in hematite photoanodes are short and that charge recombination is probable (either at the surface or in the bulk) [35]. These phenomena impair the PEC performance of hematite photoanodes considerably and so a focus has been placed on the microstructural tuning and surface treatments of such thin films to minimize carrier recombination [36].

Fig. 4.

The optical bandgap (E_g) was calculated according to the following equation:

$$\alpha\, h\nu = A^{\circ}(h\nu - E_g)^n \qquad \textbf{(3)}$$

where α is the absorption coefficient, hν is the photon energy in eV, and E_g is the band gap energy in eV. A° and n are constants that depend on the kind of electronic transition, n being equal to 1/2 and 2 for allowed direct and indirect transitions, respectively. **Fig.4b** shows the Tauc plots of $(\alpha h\nu)^2$ versus photon energy hν for α-Fe_2O_3 films deposited by AACVD for 30 min at different temperatures. The calculated bandgap of 1.99 approximately 2.00 eV was estimated from the intercept by extrapolating the linear fit of the Tauc plot to the energy axis of the film deposited at 450°C in methanol for 30min deposition time. The observed linear part of the Tauc fit indicates that the Fe_2O_3 electrodes deposited from methanol at 525 °C have a direct band gap of 1.94 eV as shown in **Fig. 4b.** The estimated bandgaps of 1.9 - 2.1 eV agree with the reported bandgap values for α-Fe_2O_3 [20, 37]. As films are deposited under varying conditions of solvent, deposition time and temperature, so the crystallinity and thickness of the Fe_2O_3 films will vary which will also impact on the optical absorption edge and bandgap [38]. The variation in film thickness affects the localized energy states which in turn changes (slightly increases or decreases) the bandgap of the material. The AACVD thin films prepared in methanol **Fig.4b** showed a slight red shift with increasing temperature for 30 min deposition time, which possibly indicates the creation of additional energy states at higher temperature.

The absorption coefficient value can be calculated from the diffuse reflectance using the Kubelka–Munk equation given below:

$$F(R) = \frac{(1-R)^2}{2RS} = K \qquad \textbf{(4)}$$

where, *R* is the absolute reflectance of the hematite nanoparticles, *K* is the molar absorption coefficient and *S* is the scattering coefficient [39]. The obtained DR-UV-Vis spectrum is converted to the Kubelka–Munk function F(R)such that the vertical axis represents the quantity $[F(R)\,h\nu]^2$, which is plotted against photon energy (hν) as shown in the **Fig. 4c**. The linear part of the curve is extrapolated, and the optical band gap energies of the films were obtained from the energy intercept, yielding values in the range of 2.05 and 2.08 eV for 20min and 30min deposition times, respectively (**Fig.4c** and inset). The calculated band gaps for the films prepared using methanol or ethanol as solvent are collated in **Table SVI.** As can be seen from **Fig. 4(c),** an apparent blue shift is observable in the reflectance spectrum of the films moving from 20min to 30min deposition time. Further, in case of ethanol solvent, increasing the preparation temperature from 450°C to 475°C leads to a decrease in the band gap from 2.08 to 1.98 eV, for 20min deposition time. However, for the films prepared for 30 min, the band gap increases from 1.97 to 2.08eV as the temperature is increased from 450 °C to 525 °C. Tauc and Kubelka-Munk plots for other films are shown in **Fig. S5.**

3.2.2. Photoelectrochemistry- linear sweep voltammetric analysis in in the absence and presence of light

The photoelectrochemical performance of the prepared α-Fe_2O_3 films was studied by recording the photocurrent density as a function of applied voltage. The experiment for all the three type of films (SP, CVD and AACVD) were performed in the dark, in continuous light and in chopped light at regular intervals. For the latter two types of experiments a source of simulated solar illumination (AM 1.5 G) under 100 mW cm^{-2} was used at 25 °C. The steady state J–V plot was superimposed on the transient plot in each case for comparative analysis. Generally, the dark current onset begins at approximately 1.7 V vs. RHE for all the electrodes in a 0.1 M NaOH electrolyte. The amount of dark current was observed to decrease with increasing film deposition temperature. The characteristic potentials at which current starts were calculated employing Nernst's equation, as reproduced below:

$$E_{RHE} = E_{Ag/AgCl} + 0.059pH + E^{0}_{Ag/AgCl} \quad \textbf{(5)}$$

where E_{RHE} is the converted potential vs. RHE, $E°_{Ag/AgCl}$ = 0.197 V at 25 °C and $E_{Ag/AgCl}$ is the experimentally measured potential against Ag/AgCl [34].

A systematic and comprehensive study was performed in order to obtain a full understanding of the behaviour of each type of film. The SP films considered were obtained from three different precursors -$FeCl_3$, $Fe(NO_3)_3.9H_2O$ and $Fe(acac)_3$ - using either methanol or ethanol, each at a deposition time of 30 min and by employing temperatures of 475°C, 500°C and 525°C (Supplementary Information; Fig. S5 and S6). **Fig. 5a-d** show the results obtained at 525°C for the three precursors in each solvent. The PEC performance of various ironoxide films along with the complete experimental conditions is given in **Table SVII**. The results show that in films from SP the photocurrent increases for all the films with different thicknesses. It has been demonstrated earlier that regulating the film thickness can balance photon absorption and charge carrier transport in order to reach higher PEC performances [39-40]. Owing to short hole diffusion length in α-Fe_2O_3 (2–4 nm), it is necessary to decrease the film thickness but decreasing film thickness may result in loss of light absorption.

Fig. 5.

It is apparent that under dark conditions the onset potential for almost all of the SP films is beyond 1.6V in both the solvents. However, in the presence of simulated sunlight (**Fig. S6)**, films fabricated from $FeCl_3$ in ethanol at a fixed deposition time at different temperatures exhibited a reduction in onset potential, with values between 1.4-1.5V. On using other precursors under similar conditions, the changes in onset potential were not substantial; $Fe(NO_3)_3.9H_2O$ gave values of 1.49-1.56 V and $Fe(acac)_3$ yielded a potential onset at 1.6 V . On switching from ethanol to methanol (with all other parameters constant) the onset values tend to be lower i.e., 0.49 V - 1.45 V for $FeCl_3$, 0.55 V - 1.44 V for $Fe(NO_3)_3$ and 0.61 V - 1.54 V for $Fe(acac)_3$. The shifts in onset potential towards less positive values at 525°C should prove beneficial for energy harvesting. To gain a better understanding of the photocurrent behaviour in films prepared under different conditions, the LSV experiments were performed under chopped light with the results shown in **Fig.5b, 5d**. From these results, the films deposited using ethanol produce a photocurrent density in the range of 0.001 - 0.05 mA cm^{-2} , 0.009 - 0.03 mA cm^{-2} and 0.005 - 0.023 mA/cm^2 for $FeCl_3$, $Fe(NO_3)_3.9H_2O$ and $Fe(acac)_3$, respectively, for three different temperatures. Notably, the current density reaches substantially higher values for the $FeCl_3$ -produced film in comparison to the films prepared from the other precursors. The current density further increases when methanol replaces ethanol, particularly for $FeCl_3$ films. The respective current density values for the films are, 0.015 mA cm^{-2}, 0.063mA cm^{-2} and 0.12mA cm^{-2} at 475, 500 and 525°C, respectively.

Fig. 6.

The representative films shown in **Fig.6** prepared by CVD methods at 500°C at different deposition times using a $FeCl_3$ precursor in either ethanol or methanol. The onset potential in the presence of light is in the range of 1.01 V - 1.17 V, with the lowest onset potential obtained from films prepared using the longest deposition period and ethanol as a solvent. A possible reason could be the passivation of surface trap states by high temperature heating treatment [23]. When studied under chopped light, the photocurrent produced by CVD films made using ethanol (Fig..6b), is found to be increase with temperature, with a maximum photocurrent of 0.123 mA cm^{-2} at 1.23 V vs. RHE. Improvements in the PEC for the films treated at higher temperatures are attributed to the improvement in crystallinity of the hematite films. Further, the annealing the films at higher temperature improved the optical absorption, as recorded above in section 2.3, which in fact is because of film densification process causing more absorption of incident photons [41]. The temperature treatment of the film decreases the inter particle distance and thus favours the electron movement, probably the electron hoping [42]. A film annealed at higher temperature provides a conduit net

which decreases the hindrance to the generated free electrons and holes and increases intrinsic carrier population which helps in fast charge transport and better conductivity. However, at the same time the agglomeration of particles also increases with increase in temperature and after certain value it may affect the PEC efficiency adversely [43].

The J-V behavior of all the rest of the prepared films prepared is shown in **Fig. S6 and Fig. S7.**

The highest photocurrent produced by any of the photoanodes prepared using methanol was approximately 0.29mA cm^{-2} at 1.23 V; i.e., more than twice that observed form similar films produced using ethanol, which indicates substantial difference in performance are imbued by switching solvent. This can presumably be explained by a complex interplay of several factors in the fabricated films, such as faster surface kinetics, improved current collection and/or enhanced light absorption. It has already been reported that methanol minimizes the surface roughness of deposited hematite films and produces smaller and smooth regular pattern of the particles [44]. Possibly this also reflects the facilitation of the formation of oxygen vacancies and consequently increases the electrical conductivity due to a greater number of photogenerated electron-hole pairs.

Fig. 7.

The photoelectrochemical performance of nanostructured α-Fe_2O_3 films prepared by AACVD at 475°C,500C & 525°C for deposition times of 20, 25 & 30 minutes in ethanol and methanol solvents using $FeCl_3$ as a precursor, was subsequently investigated. It was observed that an increase in both the deposition temperature and deposition time increases the steady-state photocurrent density.

The steady state currents in darkness and under full illumination were recorded (LSVs) for the films fabricated using ethanol at a fixed temperature with different deposition time periods as shown in **Fig. 7**(a). Generally, the dark current starts at *ca*. 1.7 V for all the electrodes in 0.1 M NaOH electrolyte. For all the electrodes prepared with ethanol over a 30 min deposition time, the photocurrent increased rapidly with onset potentials of 0.83 V,0.98 V and 0.89 V at 475°C, 500°C & 525°C, respectively (**Fig. S6**). LSVs show that for methanol-prepared films under illumination and in darkness (Fig. 7(c)), the onset potential varies from 0.75 V to 0.96 V, with the lowest potential of 0.75 V at 525°C. This corresponds to an 8.4% decrease in the onset potential as compared to films prepared with ethanol (**Fig. S6**).

In the methanol-prepared AACVD films the photocurrent increased from 0.047 mA cm^{-2} to 0.335 mA cm^{-2}, from

0.045 mA cm^{-2} to 0.673 mA cm^{-2}, and from 0.079 mA cm^{-2} to 1.23 mA cm^{-2} for processing temperatures of 475°C, 500°C & 525°C, respectively (Fig. S6). The respective current density values are 0.106, 0.24 and 1.13 mA cm^{-2} for the films prepared in ethanol (**Fig. 7(b)**). From **Fig.7(d)** it is apparent that the electrode deposited at 525 °C, prepared using methanol delivered the highest current density of 1.23 mA cm^{-2} at 1.23 V. Importantly, this value also represents the highest photocurrent density recorded among any of the hematite films, irrespective of preparation method (i.e. SP vs. CVD vs. AACVD). This increased photocurrent density at 525 °C can take values of 1.23 -1.32 mA cm^{-2} when the potential is raised from 1.23 V towards 1.27 V. The observed photocurrent maximum can be interpreted in terms of a large active surface area due to smaller particles and hence a more effective semiconductor for photoelectrochemical cell. The photocurrent data for the remaining films are provided in the supplementary information (**Fig. S7**). In very few samples the photocurrent in continuous light was found higher than that of the same film in chopped light which was attributed to surface changes during the experiment. However, the calculations are always based on lower photocurrent values.

The evidence of the higher photocurrent that can be obtained at higher potentials for films deposited over 30 mins (e.g., 1.23mA cm^{-2} at 1.23 V and 1.32mA cm^{-2} at 1.27 V when using methanol and heating at 525°C) clearly shows the importance of deposition time. This is ascribed to the improvement in film structure leading to higher crystallinity as indicated by PXD analysis. One would expect these well sintered, denser, crystalline films to exhibit superior transport properties. The resulting α-Fe_2O_3 film morphology also provides a better interface between the electrode and the electrolyte for rapid charge transfer. The relevant diffusion distances are sufficiently short for the photogenerated holes to reach the electrolyte rapidly, suppressing their recombination.

The observed increase in photocurrent with the increase in film deposition temperature tends to indicate further improvements in film structure. At higher processing temperatures there would be a greater driving force to reorient adjacent grains of hematite and to remove grain boundaries, thus further facilitating electronic transport within the hematite film. In fact, the photocurrent density of the optimized AACVD α-Fe_2O_3 thin films (of 1.23mA cm^{-2} at 1.23 V vs. RHE) is to the best of our knowledge, the highest photocurrent reported to date for any pristine (externally un-doped) hematite thin film prepared by the AACVD method. By comparison, a photocurrent of 455μA cm^{-2} at 1.23 V vs. RHE at 450°C was reported for a nanostructured α-Fe_2O_3 AACVD thin film in 2014 [20], while in 2019, a current density of 585 μA cm^{-2} at 1.2 V vs Ag/AgCl was recorded for an AACVD hematite film [21].

This impressive PEC performance of AACVD thin films would seem to be generally attributable to the improved crystallinity of hematite nano-elliptical thin films with enriched (110) facets (Fig. 1a & b) and their consequent excellent light harvesting property. Despite a hole diffusion length of the order 2–4 nm [21] the tuning of the thin film nanostructure substantially affects the photocurrent. The electron-hole (e-h) separation within the width of the space charge layer becomes a key factor, which seems to be more pronounced for electrodes composed of films deposited at higher temperature (in our case, at 525 °C). **Table SVII** compares the PEC performance (e.g., in terms of lowest onset potential and highest photocurrent density at 1.23 V vs. RHE) of an extended selection of photoanodes with respect to fabrication method and key processing parameters.

The stability of the prepared photoanode in PEC water splitting is crucial for both fundamental and practical studies **Fig. 7e** contrasts the photocurrent curves of optimized AACVD α-Fe_2O_3 photoanodes fabricated with either methanol or ethanol measured at 1.23 V *vs.* RHE in a 0.1 M NaOH electrolyte under AM 1.5 illumination for 2.7 h. Although the photocurrent of the α-Fe_2O_3 photoanode varies from 0.145 mA cm^{-2} to 0.283 mA cm^{-2} and from 0.78 mA cm^{-2} to ~1.08 mA cm^{-2}, in ethanol and methanol, respectively there is no steady decline with time; in fact the current density fluctuates in a rather irregular manner. After 2.7 h the photocurrent is more than 90% of the initial value indicating that despite the observed fluctuations, both photoanodes exhibited very satisfactory stability during PEC water splitting.

The observed slight decrease in initial current density over time could be due to gas bubble accumulation, which was observed on the surface of the electrode during the test. The gas bubbles tend to adhere to the electrode surface, thus decreasing the effective available electrode area and increasing the interfacial electric resistance [45], which causes a decrease in current density. Further, a reduction in photocurrent density could arise from space charge accumulation on the surface of the film which creates a barrier to the reaction by preventing the charges accommodated by the electrolyte.

3.2.3. Electrochemical impedance spectroscopy (EIS) - charge transport dynamics

Charge transport kinetics and the interfacial dynamics were analyzed using EIS measurements performed on bare hematite photoanodes in order to try to understand the phenomena, such as deviations in photocurrent density, that we had observed. **Fig. 8 (a &b)** shows the impedance spectra obtained for the PEC cell in a three-electrode configuration

both in darkness and under illumination, the inset shows the actual shape of the spectrum in light for small impedance region. The spectra were analyzed in terms of charge transfer at the electrode-electrolyte interface.

On comparison of the Nyquist plots made from data taken in darkness and under illumination (**Fig 8a**) it is apparent that quite different impedance responses were obtained. The plot of data taken under illumination shows a semicircle (see the inset in Fig.8a) for the bare photoanode with much reduced impedance, negligible compared to the equivalent date collected in darkness. Generally, the high frequency semicircle describes the charge-transfer process in the semiconductor depletion layer and estimates the trapping of the photogenerated charges in the bulk of photoanode. By contrast, the semicircle in the low frequency region can be attributed to the electron transfer at the Helmholtz layer associated with the phenomenon of a change in surface states [46]. A decrease in the resistance of the α-Fe_2O_3 films in light indicates the ability of the electrode to produces a far higher current that is sufficient for water splitting. The noisy feature in the low frequency region of Bode plot is likely due to the surface morphological changes of the films.

It is well established that a space charge layer can arise between an electrolyte solution and a semiconducting electrode in an electrochemical cell under conditions of darkness [47]. An equilibrium between the electrochemical potentials of the two phases is established owing to the charge transfer process across the interface. The development of a positive space charge layer against the negative charge layer at the two sides of the electrode-electrolyte junction leads to the development of a depletion layer. This creates a potential gradient on the semiconductor side due to the arrangement of ions in the Helmholtz layer that develops. Upon illumination, photons with a threshold energy (greater than the band gap) absorbed on the surface produce e-h pairs. Those absorbed in the depletion layer are also able to generate e-h pairs by means of electric field generation. Consequently, the Fermi level of the semiconductor shifts towards its flat-band potential to attain its original equilibrium [48].

The corresponding Bode plots are shown in **Fig. 8b,** depicting the typical phase angle and total impedance profile versus scanned frequency range. The higher frequency peak in the Bode-phase diagram corresponds to the depletion layer, whereas the peak at lower frequency corresponds to the Helmholtz layer. The electrolyte layer adjacent to the solid/liquid interface which corresponds to a much lower impedance compared to that of the bulk [48], is analyzed.

Fig. 8

due to its involvement in the photocurrent generation. In darkness, the diffusion of ions within the electrolyte solution is a mass transport process and is indicated by a Warburg element in the equivalent circuit of the EIS pattern [49]. Under illumination the mass transport is no longer based on a Nernst diffusion process; therefore, it cannot be modeled by a Warburg impedance. The absence of a linear contribution to the impedance at low frequency in the Nyquist plot (as a 45° diagonal line), also suggests the absence of mass transport. In darkness the observed higher resistance is due to the equilibrium of charges but in simulated sunlight the produced electrons pass to the external circuit due to the photoexcitation of the conduction band electrons which show very low negligible resistance as is evident from the impedance spectrum.

The Bode plot of the modulus impedance clearly depicts a decrease in resistance on moving to the high frequency region. Looking at the phase spectrum, two processes can be recognized in the lower and higher frequency regions, respectively. Namely the charge transfer at the solid/liquid interface (Helmholtz layer) and the charge transport inside the film (depletion layer). The increase in voltage accelerates the charge transfer and is reflected in the peak shift toward higher frequencies and is finally comparable with that of the other process for potentials larger than 0.6 V vs. Ag/AgCl (the onset potential). The facilitation of charge transfer process at higher potential is ascribed to the increase in surface states which can be interpreted as the charge transfer mechanism [48-50].

To generate a quantitative interpretation of the charge carriers produced, the electron lifetime (τ_e) was calculated from equation (6) below [51]. The electron lifetime (τ_e) in the pristine hematite films was thus obtained from the characteristic angular frequency (ω_{mid}) of the middle frequency (f_{mid}) peak in the Bode phase plots.

$$\tau_e = (1/(2\pi\omega_{mid}) \qquad \textbf{(6)}$$

An electron lifetime of 175 µs was obtained for the film prepared by AACVD method in methanol at 525Cin 0.1M NaOH. The lifetime is considerably higher than the majority of previously reported values which are typically in the range of 2 to 2.5 µs [52]. A very notable exception, however, is presented in the recent work by Subramaanian et al. where an electron lifetime of 1.09 ms was demonstrated to exist. This extraordinary electron lifetime possibly originated from the surface treatment of FeOOH and by employing the significantly higher film annealing temperature of 800 ^{o}C [53].

3.3. Hydrogen evolution measurements:

Fig. 8c shows the hydrogen generation performance of the Fe_2O_3 photoelectrode in an aqueous 0.1 M NaOH solution under constant illumination. The photoelectrochemical water splitting was monitored in a custom-made glass reactor vessel attached to a fused silica viewport as described in the experimental section. The hematite photoanode, which acted as the working electrode, and the Pt counter electrode were connected directly by a single looped wire, without any external bias. Gas evolution measurements was performed for several selected films prepared by AACVD methods and optimized results are shown in **Fig. 8c** above. Further data are reported in **Table SVIII**.

The observed amount of O_2 evolved is less than expected probably due to unanticipated gas leakage during the sampling and manual injection into the GC. Secondly, being the limiting nature of the oxygen reduction reaction (ORR), which accompanies with hydrogen evolution reaction (HER) on cathode surface could also be a reason for this decrease. Nevertheless, most of the photogenerated holes were consumed for oxygen production in the PEC setup. The amount of oxygen gas produced spontaneously from water splitting at the α- Fe_2O_3 photoanode was quantified for the first 6 h cycle as 1.2 μmol cm^{-2} while the corresponding amount of hydrogen evolved was 0.4 μmol cm^{-2} (**Fig.8c**). By way of comparison, in 2018 hematite nanorods annealed in Argon gas at 500 °C produced 45 μmol cm^{-2} of oxygen gas in 2 h [16], whereas in 2019, a Ti-modified hematite photoanode produced 2.5 μmol cm^{-2} of oxygen in 3 h [37].

There is an obvious correlation between the considerable amount of hydrogen produced by the electrode and the significant photocurrent that it produces (as seen in the J-V curves); enough electrons are generated to produce relatively abundant hydrogen. That the amount of hydrogen evolved was not even higher suggests that some of the generated electrons may not have been able to contribute to the production of hydrogen gas due to competing recombination processes. Two probable reasons for the decreased hydrogen generation could be: (a) that the dense morphology of the films adversely affected the penetration of the electrolyte into the film and (b) that bubbles accumulate as they form at the photoelectrode. These bubbles adhere to the electrode surface, decreasing the effective surface area and introducing additional surface resistance, thus increasing the chances of charge recombination. Both these issues are worthy of further investigation and should accordingly be addressed by appropriate surface treatment of the thin films.

4. Conclusions

Thin films of pristine hematite (α-Fe_2O_3) have been developed by three different deposition techniques, i.e., SP, CVD, and AACVD, as photoanodes for electrochemical water splitting. The results of PXD, RAMAN and SEM manifestly showed that single phase films could be obtained at 525°C with no evidence of undesired impurity phases such as Fe(II)-containing FeO and Fe_3O_4. The films prepared by the AACVD method produced remarkably high photocurrent density compared to the films prepared by the other two deposition methods. Moreover, to the best of our knowledge, optimized AACVD photoanodes (produced at a relatively low temperature of 525 ^oC) were able to generate the highest photocurrent density of any pristine hematite thin film reported to date (of 1.23 mA cm^{-2} at 1.23 V vs. RHE) with an onset potential approximately twice as low as any previous equivalent electrode. Encouragingly, the photoanodes prepared by SP and CVD methods also showed improved photocurrent generation in comparison to many previously reported pristine hematite electrodes prepared using similar methodologies. The selected thin film electrodes showed a 92% retention of photocurrent after continuous exposure to light for 6 h, thus demonstrating competitive photoelectrochemical stability. Electrochemical impedance spectroscopy revealed low electrical resistances and fast charge transfer kinetics on these films suggesting that photogenerated holes and electrons could diffuse to the electrolyte interface considerably faster than they could recombine. The photoelectrochemical generation of oxygen (1.2 μmol cm^{-2}) on the photoanode and that of hydrogen (0.4 μmol cm^{-2}) on the Pt counter electrode was established qualitatively and quantitatively over a 6 h duration.

Future work: In the continuity of this work the study of surface properties and doped analogues (e.g. TiO_2, C) of the α-hematite cold be an interesting research with AACVD method. Work is in progress in our lab on these lines.

Acknowledgment: We are very grateful to the Higher Education Commission (HEC) of Pakistan for financial support through a 6-month scholarship to S.Qureshi to visit the University of Glasgow under the International Research Support Initiative Program (IRSIP; No. *1-8/HEC/HD/2017/8222*).

Conflict of interest: The authors declare that they have no conflict of interest.

References:

1. A. G. Tamirat, J. Rick, A. A. Dubale, W. N. Su, B. J. Hwang, Using hematite for photoelectrochemical water splitting: a review of current progress and challenges. Nanoscale Horiz. 1, 243 (2016).
2. S. Y. Tee, K. Y. Win, W. S. Teo, L. D. Koh, S. Liu, C. P. Teng, M. Y. Han. Recent progress in energy- driven water splitting. Adv. Sci. 4, 1600337 (2017).
3. P. S. Bassi, T. Sritharan, L. H. Wong. Recent progress in iron oxide based photoanodes for solar water splitting. J. Phys. D Appl. Phys. 51, 473002 (2018).
4. T. Liu, M. Morelli, Y. Li. Photoelectrochemical Solar Cells, ed. by N.D. Sankir, M. Sankir (Wiley, Beverly, MA, 2018), p.159.
5. K. Sivula, F. Le Formal, M. Grätzel, Solar water splitting: Progress using hematite (α- Fe_2O_3) photoelectrodes. ChemSusChem. 4,432, (2011).
6. P. S. Bassi, L. H. Wong, J. Barber. Iron based photoanodes for solar fuel production. Phys. Chem. Chem. Phys. 16, 11834 (2014).
7. J. Y. Kim, G. Magesh, D. H. Youn, J. W. Jang, J. Kubota, K. Domen, J. S. Lee. Sci Rep. 3, 2681 (2013).
8. R. Zhang, L. Yang, X. Huang, T. Chen, F. Qu, Z. Liu, & X. Sun. Se doping: an effective strategy toward Fe_2O_3 nanorod arrays for greatly enhanced solar water oxidation. J. Mater. Chem. A 5, 12086 (2017).
9. O. Zandi, B. M. Klahr, T. W. Hamann. Highly photoactive Ti-doped α- Fe_2O_3 thin film electrodes. Energ. Environ. Sci. 6, 634 (2013).
10. S. Kment, Z. Hubicka, J. Krysa, D.Sekora, M. Zlamal, J. Olejnicek, R. Zboril. On the improvement of PEC activity of hematite thin films deposited by high-power pulsed magnetron sputtering method. Appl. Catalysis B:Env.165, 344 (2015).
11. L. Zhao, J. Xiao, H. Huang, Q. Huang, Y. Zhao, Y. Li. Enhanced efficiency of hematite photoanode for water splitting with the doping of Ge. Int. J. Hydrogen Energy. 43, 12646 (2018).
12. F. Wang, L. Song, H. Zhang, L. Luo, D. Wang, J. Tang. One-dimensional metal-oxide nanostructures for solar photocatalytic water-splitting. J. Electron. Mater. 46, 4716 (2017).
13. G. Rahman, O. S. Joo, S. Y. Chae, A. H. Shah, S. A. Mian. Enhanced water oxidation photoactivity of nano-architectured α-Fe_2O_3-WO_3 composite synthesized by single-step hydrothermal method. J. Electron. Mater. 47, 2359 (2018).

14. G. Kaura, Divya, S. A. Khan, V. R. Satsangi, S. Dass, R, Shrivastav. Nano-hetero-structured thin films, ZnO/Ag-(α) Fe_2O_3, with n/n junction, as efficient photoanode for renewable hydrogen generation via photoelectrochemical water splitting. Renew. Energy. 164, 156 (2021).
15. P. Liu, C. Wang, L. Wang, X. Wu, L. Zheng, H. G. Yang. Ultrathin hematite photoanode with gradient Ti doping. Research 2020, 5473217 (2020).
16. X. Wang, W. Gao, Z. Zhao, L. Zhao, J. P. Claverie, X. Zhang, J. Wang, H. Liua, Y. Sang. Efficient photo-electrochemical water splitting based on hematite nanorods doped with phosphorus. Appl. Catal. B-Environ. 248, 388 (2019).
17. C. Feng, S. Fu, W. Wang, Y. Zhang, Y. Bi. High-crystalline and high-aspect-ratio hematite nanotube photoanode for efficient solar water splitting. Appl. Catal. B-Environ. 257, 117900 (2019).
18. J. Deng, Q. Zhuo, X. Lv. Hierarchical TiO_2/Fe_2O_3 heterojunction photoanode for improved photoelectrochemical water oxidation. J. Electroanal. Chem., 835, 287 (2019).
19. D. Chen, Z. Liu, S. Zhang. Enhanced PEC performance of hematite photoanode coupled with bimetallic oxyhydroxide NiFeOOH through a simple electroless method. Appl. Catal. B: Environmental, 265, 118580 (2020).
20. A. A. Tahir, M. A. Mat- Teridi, K. U. Wijayanth. Photoelectrochemical properties of texture- controlled nanostructured α- Fe_2O_3 thin films prepared by AACVD. pss (RRL) 8, 976 (2014).
21. N. A. Arzaee, M. F. Noh, A. Ab Halim, M. A. Rahim, N. A. Mohamed, J. Safaei, A. Aadenan, S. N. Nasir, A. F. Ismail, M. A. Teridi. Cyclic voltammetry-A promising approach towards improving photoelectrochemical activity of hematite. Ceram. Int. 45, 16797 (2019).
22. G. S. Pawar, A. A. Tahir. Unbiased spontaneous solar fuel production using stable $LaFeO_3$ photoelectrode. Sci. Rep. 8, 1 (2018).
23. A. Martinez, J. Pena, M. Labeau, J. M. Gonzalez-Calbet, M. Vallet-Regi. The deposition of α–Fe_2O_3 by aerosol chemical vapor deposition. J. Mater. Res. 10,1307 (1995).
24. P. Scherrer. Estimation of the size and internal structure of colloidal particles by means of Röntgen rays. Göttinger Nachrichten Math. Phys. 2, 98 (1918).
25. H. S. Choi, S. W. Rhee. Effect of Carrier Gases on the Chemical Vapor Deposition of Tungsten from WF6-SiH_4. J. Electrochem. Soc. 141, 475 (1994).

26. D. Peeters, A. Sadlo, K. Lowjaga, O. Mendoza Reyes, L. Wang, A. Devi. Nanostructured Fe_2O_3 processing via water- assisted ALD and low- Temperature CVD from a versatile iron ketoiminate precursor. Adv Mater. Interfaces, 4, 1700155 (2017).

27. C. S. Enache, Y. Q. Liang, R. Van de Krol. Characterization of structured α-Fe_2O_3 photoanodes prepared via electrodeposition and thermal oxidation of iron. Thin Solid Films 520, 1034 (2011).

28. J. A. Morales-Morales. Synthesis of hematite a-Fe_2O_3 nano powders by the controlled precipitation method. Cienc en Desarro 8, 99 (2017).

29. M. Hanesch. Raman spectroscopy of iron oxides and (oxy) hydroxides at low laser power and possible applications in environmental magnetic studies. Geophys. J. Int. 177, 941 (2009).

30. D. L. De Faria, S. Venâncio Silva, M. T. De Oliveira. Raman microspectroscopy of some iron oxides and oxyhydroxides. J. Raman Spectrosc. 28, 873 (1997).

31. X. Su, C. Yu, C. Qiang. Synthesis of α-Fe_2O_3 nanobelts and nanoflakes by thermal oxidation and study to their magnetic properties. Appl. Surf. Sci. 257, 9014 (2011).

32. S. H. Shim, T. S. Duff. Raman spectroscopy of Fe_2O_3 to 62 GPa. Am. Mineral. 87, 318 (2002).

33. S. S. Shinde, R. A. Bansode, C. H. Bhosale, K. Y. Rajpure. Physical properties of hematite α-Fe_2O_3 thin films: J. Semicond 32, 013001 (2011).

34. S. Shen, S. A. Lindley, X. Chen. Hematite heterostructures for photoelectrochemical water splitting: rational materials design and charge carrier dynamics. J. Z. Zhang, Energy Environ. Sci. 9, 2744 (2016).

35. D. A. Wheeler, G. Wang, Y. Ling, Y. Li, J. Z. Zhang. Nanostructured hematite: synthesis, characterization, charge carrier dynamics, and photoelectrochemical properties. Energy Environ. Sci. 5, 6682 (2012).

36. Z. Zhang, I. Karimata, H. Nagashima, S. Muto, K. Ohara, K. Sugimoto, T. Tachikawa. Over 16% efficiency organic photovoltaic cells enabled by a chlorinated acceptor with increased open-circuit voltages. Nat. Commun. 10, 1 (2019).

37. R. Singaravelan, S. B. Alwar. Electrochemical synthesis, characterization, and phytogenic properties of silver nanoparticles. Appl. Nanosci. 5, 983 (2015).

38. B. Abdullah, A. Ismail, H. Kashoua, W. Zetoun. Effects of deposition time on the morphology, structure, and optical properties of PbS thin films prepared by chemical bath deposition. Journal of Nanomaterials, 2018, 1826959 (2018).

39. M. Vanags, A. Sukta, J. Kleperis, P. Shipkovs. Comparison of the electrochemical properties of hematite thin films prepared by spray pyrolysis and electrodeposition. Ceram. Int., 41, 9024 (2015).

40. S. Shen, C. X. Kronawitter, D. A. Wheeler, P. Guo, S. A. Lindley, J. Jiang,S. S. Mao. Physical and photoelectrochemical characterization of Ti-doped hematite photoanodes prepared by solution growth. J. Mater. Chemistry A, 1, 14498 (2013).

41. L. P. de Souza, R.O.G. Chaves, A. Malachias, R. Paniago, S.O. Ferreira, A.S. Ferlauto. Influence of annealing temperature and Sn doping on the optical properties of hematite thin films determined by spectroscopic ellipsometry. J. Appl. Phys. 119, 245104 (2016).

42. K. Sivula, R. Zboril, F. Le Formal, R. Robert, A. Weidenkaff, J. Tucek, J. Frydrych, M. Gratzel. Photoelectrochemical water splitting with mesoporous hematite prepared by a solution-based colloidal approach. J. Am. Chem. Soc. 132, 7436 (2010).

43. E. S. Cho, M. J. Kanga, Y.S. Kang. Enhanced photocurrent density of hematite thin films on FTO substrates: effect of post-annealing temperature. Phys. Chem. Chem. Phys.17, 16145 (2015).

44. K. L. Foo, M. Kashif, U. Hashim, W. W. Liu. Effect of different solvents on the structural and optical properties of zinc oxide thin films for optoelectronic applications. Ceram. Int. 40, 753 (2014).

45. S. Hernández, G. Barbero, G. Saracco, A. L. Alexe-Ionescu. Considerations on oxygen bubble formation and evolution on $BiVO_4$ porous anodes used in water splitting photoelectrochemical cells. J. Phys. Chem. C. 119, 9916 (2015).

46. T. Lopes, L. Andrade, F. Le Formal, M. Gratzel, K. Sivula, A. Mendes. Hematite photoelectrodes for water splitting: evaluation of the role of film thickness by impedance spectroscopy. Phys. Chem. Chem. Phys. 16, 16515 (2014).

47. P. S. Bassi, L. Xianglin, Y. Fang, J. S. Loo, J. Barber, L. H. Wong. Understanding charge transport in non-doped pristine and surface passivated hematite (Fe_2O_3) nanorods under front and backside illumination in the context of light induced water splitting. Phys. Chem. Chem. Phys. 18, 30370 (2016).

48. T. Lopes, L. Andrade, H. A. Ribeiro, A. Mende. Characterization of photoelectrochemical cells for water splitting by electrochemical impedance spectroscopy. Int. J. Hydrogen Energy. 35, 11601 (2010).

49. A. Boudjemaa, S. Boumaza, M. Trari, R. Bouarab, A. Bouguelia. Physical and photo-electrochemical characterizations of α-Fe_2O_3. Application for hydrogen production. Int. J. Hydrogen Energy. 34, 4268 (2009).

50. L. Xi, C. Schwanke, D. Zhou, D. Drevon, R. van de Krol, K. M. Lange. In situ XAS study of CoB i modified hematite photoanodes. Dalton Trans. 46, 15719 (2017).

51. A. Aruchamy, G. Aravamudan, G. S. Rao. Semiconductor based photoelectrochemical cells for solar energy conversion-an overview. B. Mater. Sci. 4, 483 (1982).

52. Y. Lin, G. Yuan, S. Sheehan, S. Zhou, D. Wang, Hematite-Based Solar Water Splitting: Challenges and Opportunities. Energy Environ. Sci. 4, 4862 (2011).

53. A. Subramanian, M. A. Mahadik, J.W. Park, I. K. Jeong, H. S. Chung, H. H. Lee, S. H. Choi, W. S. Chae, J. S. Jang. An effective strategy to promote hematite photoanode at low voltage bias via Zr^{4+}/Al^{3+} co-doping and CoOx OER co-catalyst. Electrochim. Acta 319, 444 (2019).

Figure Captions:

Fig.1. Representative PXD patterns from films prepared by using $FeCl_3$ precursor in methanol annealed at 525° C by; (a) CVD and SP method with standard JCPDS card # 00-024-0072 (b) AACVD method at different processing temperatures.

Fig. 2. Raman spectra of hematite thin films in (a) ethanol and (b) in methanol at 450-525°C for 30 minutes deposition time by AACVD at different temperatures.

Fig. 3. SEM images of hematite thin films prepared at 525°C from $FeCl_3$ by (a) SP (b) CVD and (c) AACVD methods; (d) cross sectional image of the film prepared by AACVD method.

Fig. 4. (a) Absorbance spectra of iron oxide films prepared from $FeCl_3$ in methanol at different temperatures for 30 minutes by the AACVD method; (b) Tauc plots taken from the absorption spectral data; (c) Kubelka – Munk plots using absorption data for the calculation of sample band gaps.

Fig. 5. LSVs, in 0.1M NaOH at $10mVs^{-1}$, in darkness, under illumination and in chopped light for the α-hematite films prepared by spray pyrolysis at 525°C using three different precursors: (a & b) in ethanol and (c & d) in methanol solvent .

Fig. 6. LSVs, in 0.1M NaOH at $10mVs^{-1}$, for iron oxide thin films fabricated by CVD using $FeCl_3$ in (a & b) ethanol and (c &d) in methanol at 500 °C for different film deposition times. LSVs conducted in darkness and under illumination (a,c) and under chopped light (b,d) are shown.

Fig. 7. LSVs, in 0.1M NaOH at $10mVs^{-1}$, for hematite thin films fabricated at 525 °C by the AACVD method using $FeCl_3$ and (a & b) ethanol or (c &d) methanol for different film deposition times. LSVs are taken in darkness and under full illumination in (a, c) and under chopped light in (b, d), comparative photocurrent stability plots of AACVD films fabricated from $FeCl_3$ at 525°C using methanol and ethanol with 30 min deposition time (e).

Fig. 8 EIS analysis of optimized hematite thin films prepared by AACVD using methanol at 525°C (a) Nyquist plots (b) Bode plots. (c) Plot of evolved hydrogen and oxygen as a function of time over 6 h, using an optimized hematite electrode in aqueous 0.1 M NaOH.

Figure 1

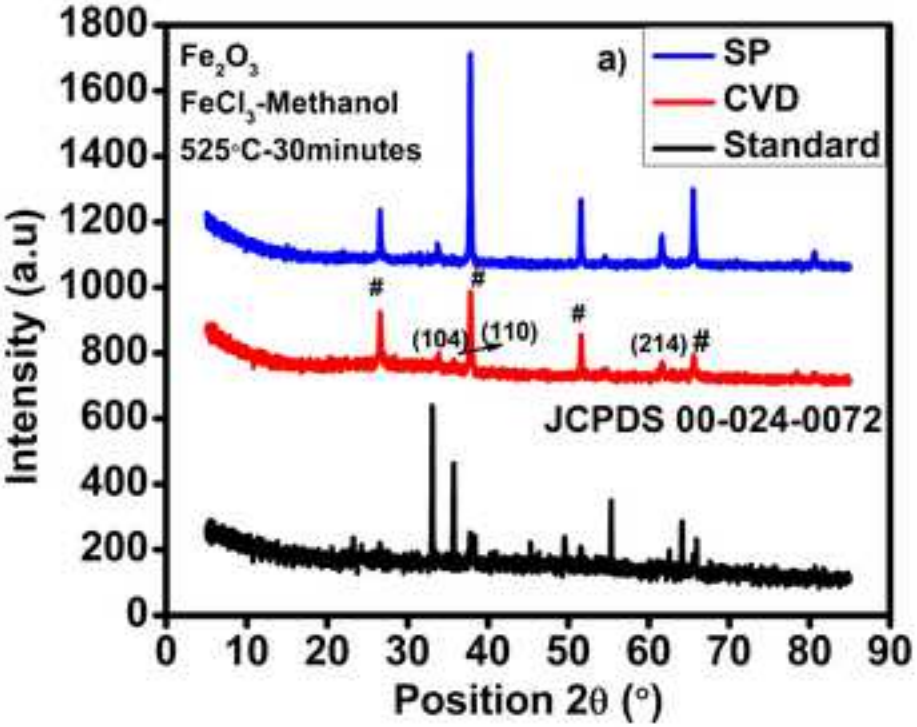

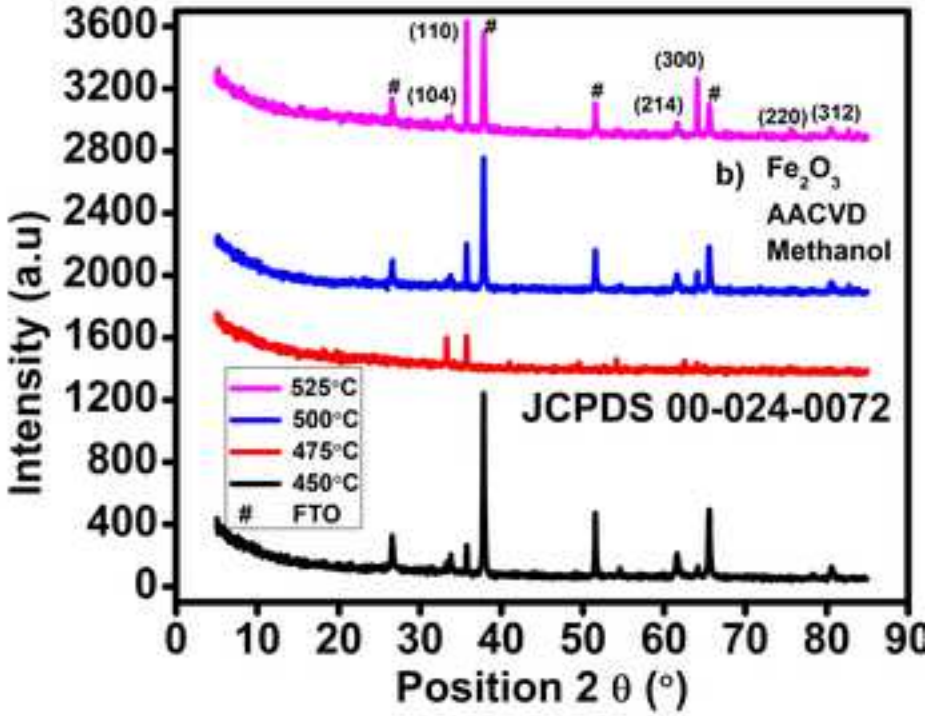

Figure 2

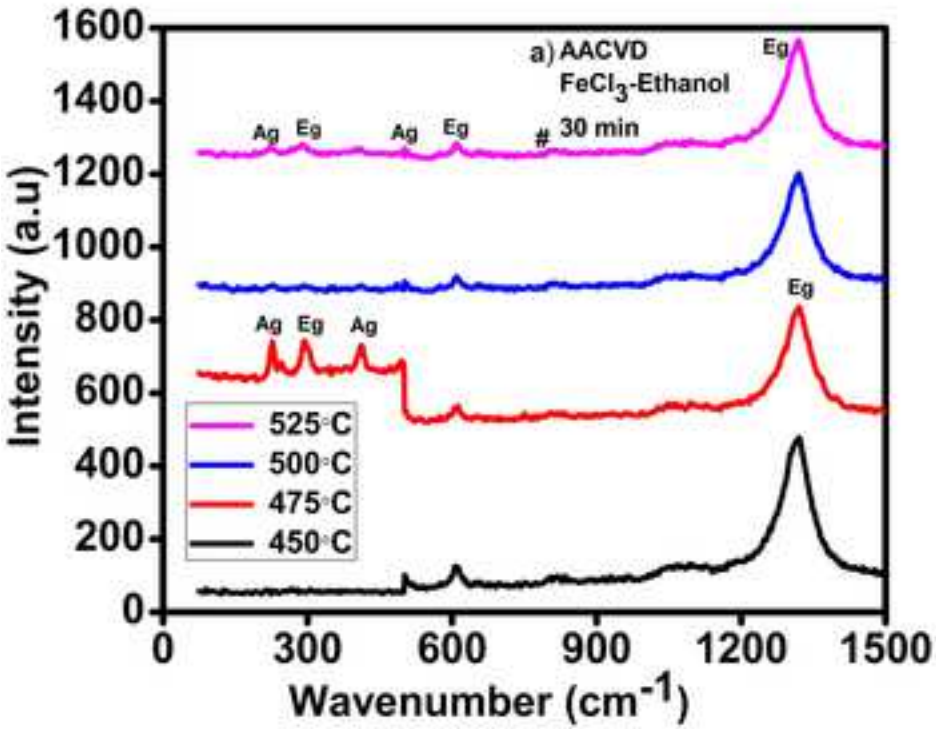

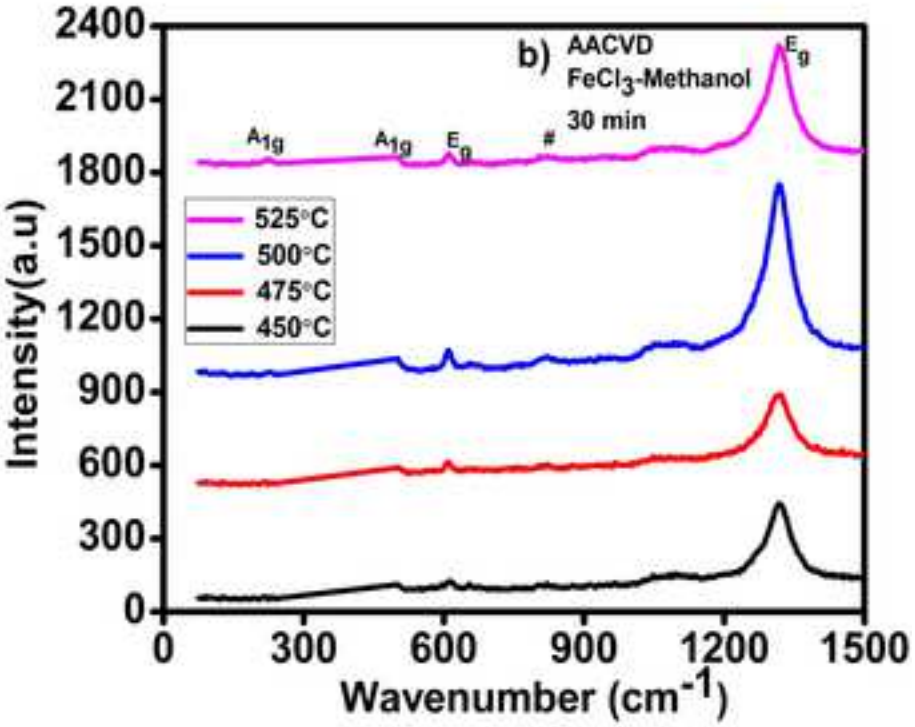

Figure 3

Click here to access/download;Figure;Fig.3.jpg

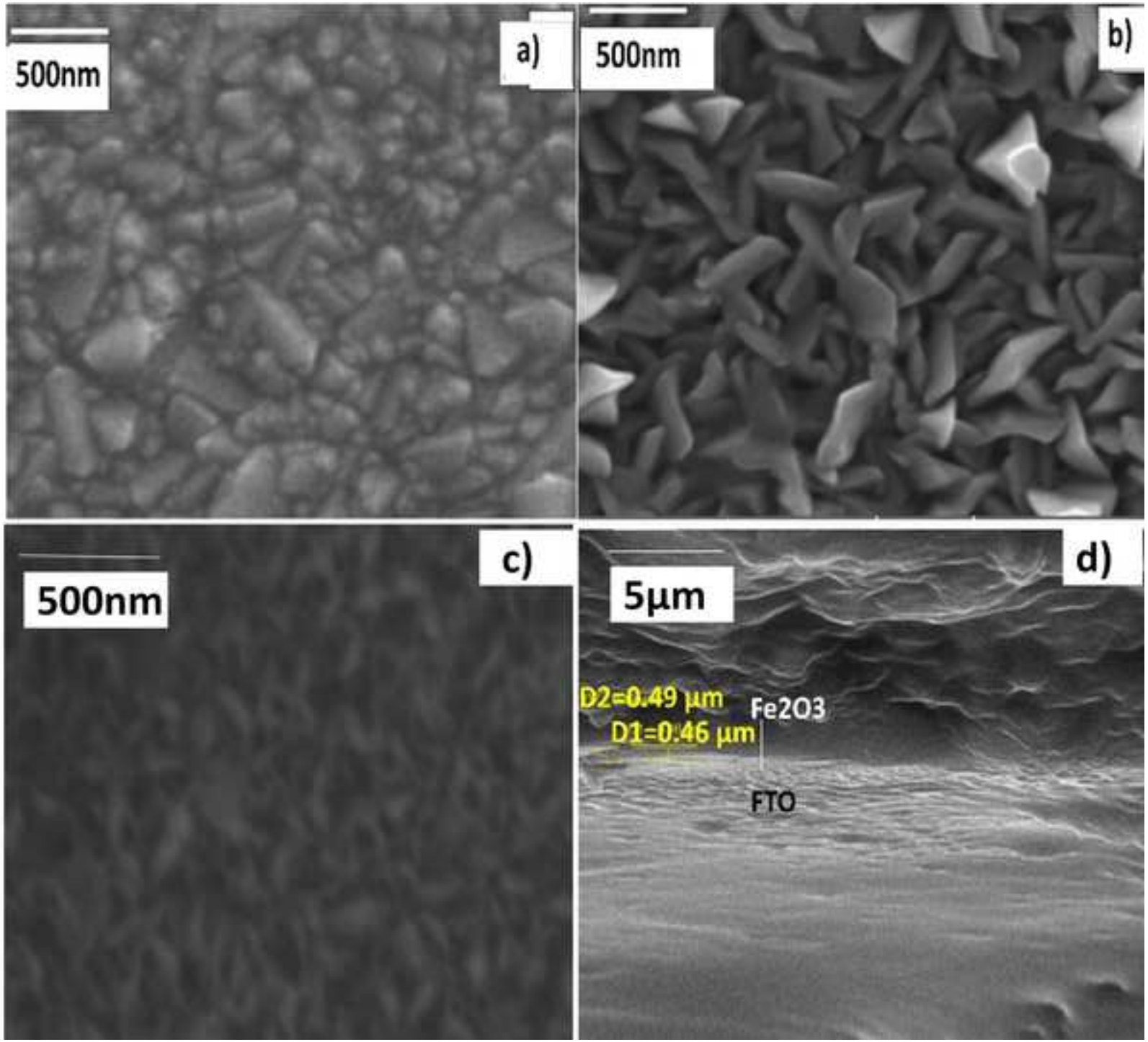

Figure 4

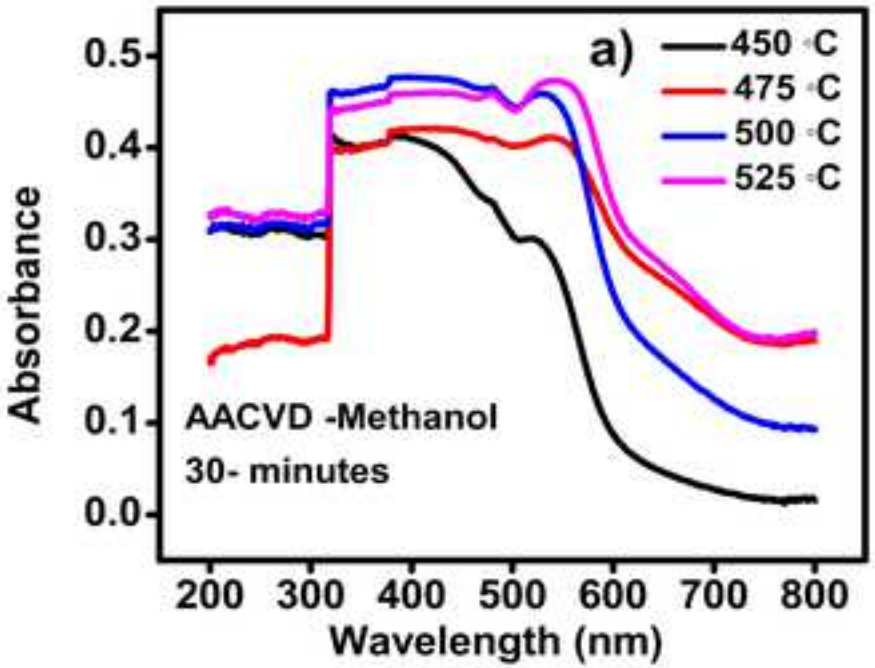

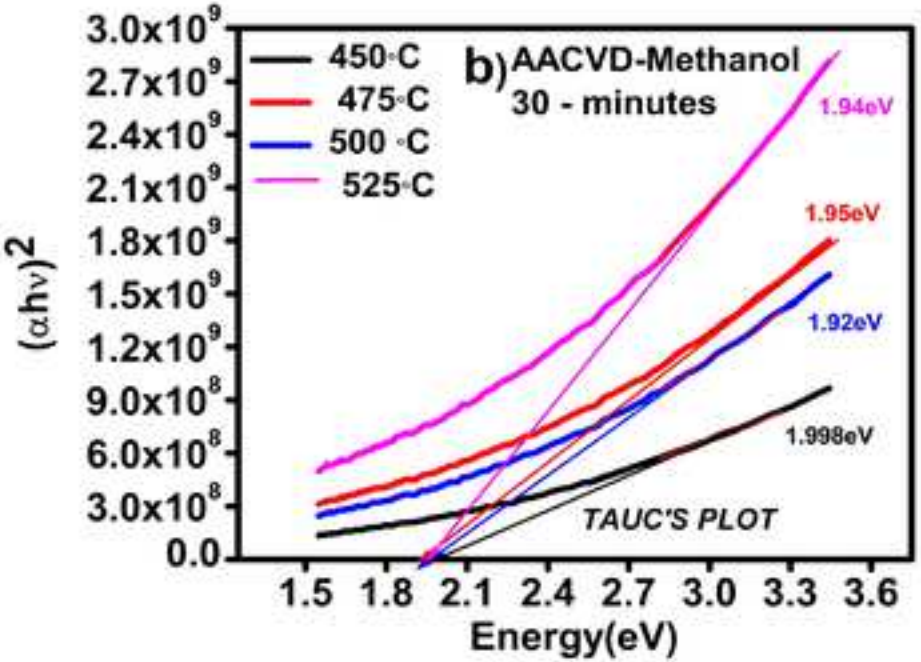

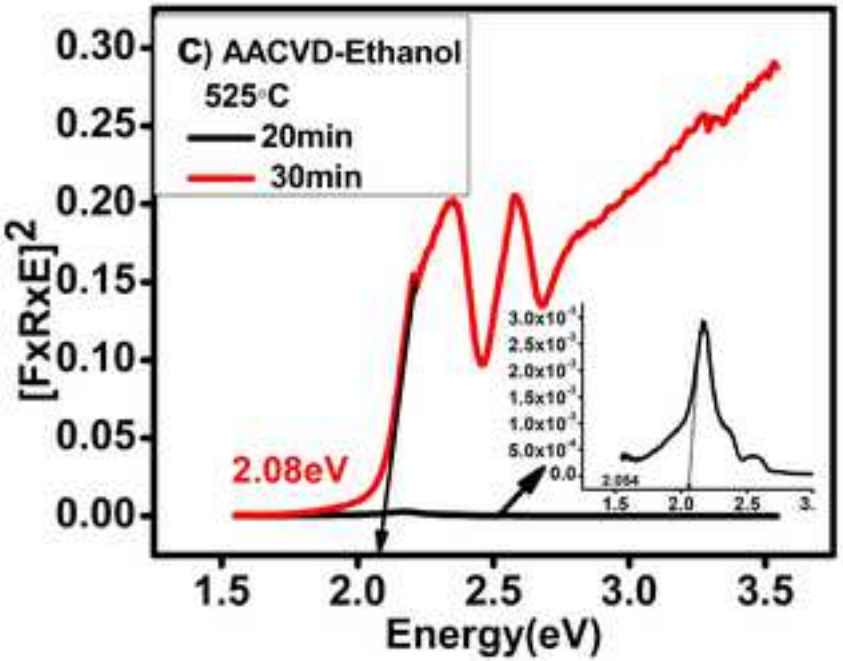

Figure 5

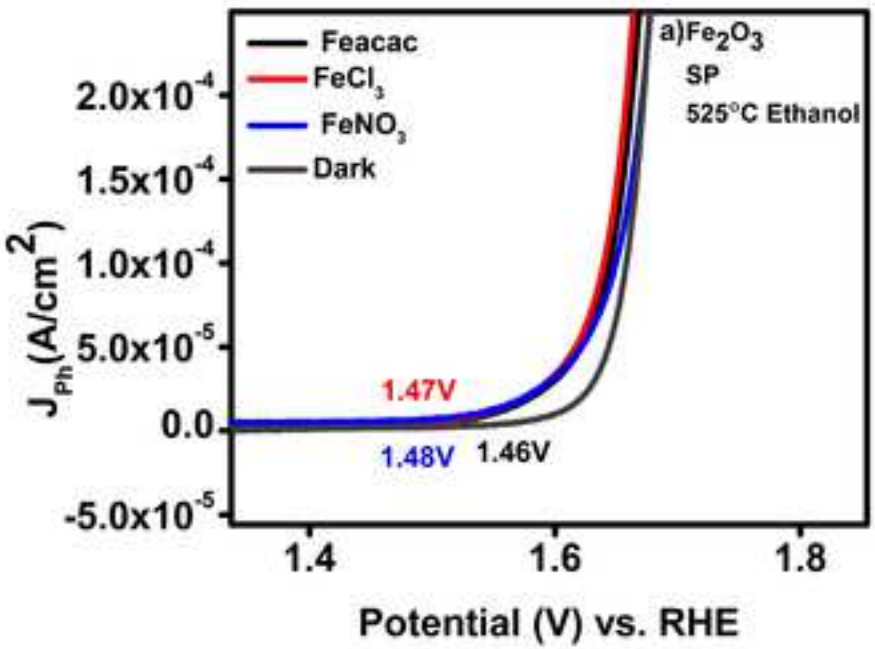

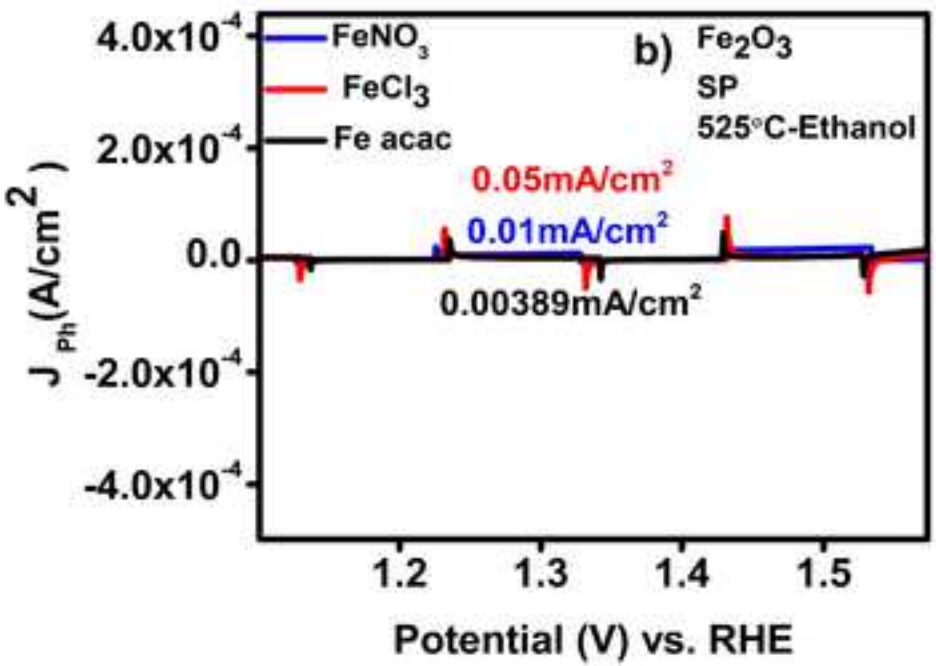

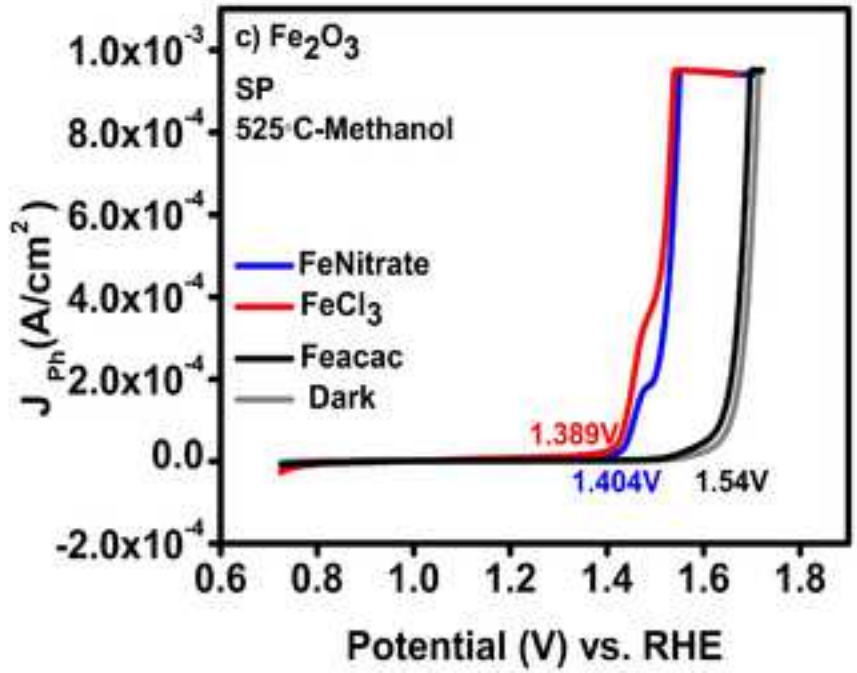

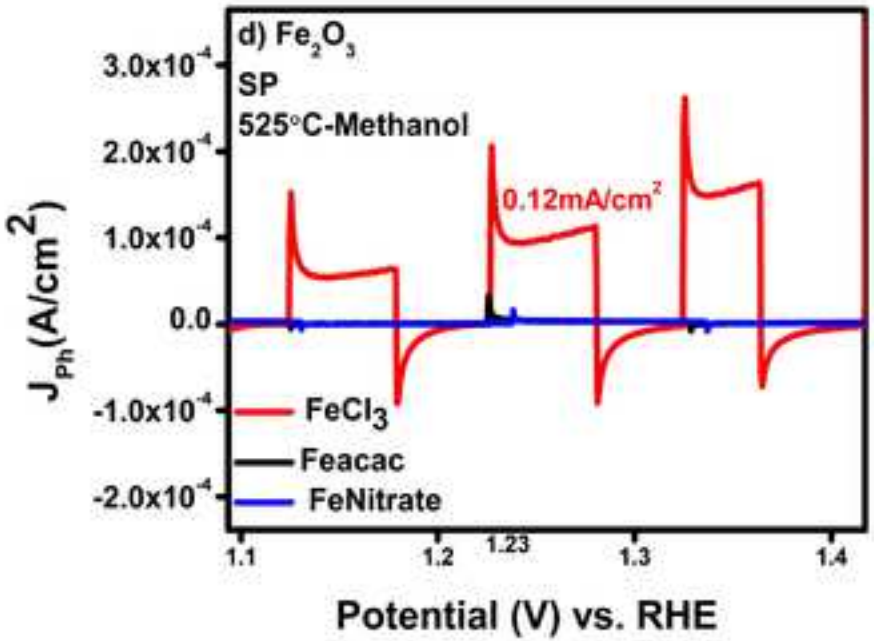

Figure 6

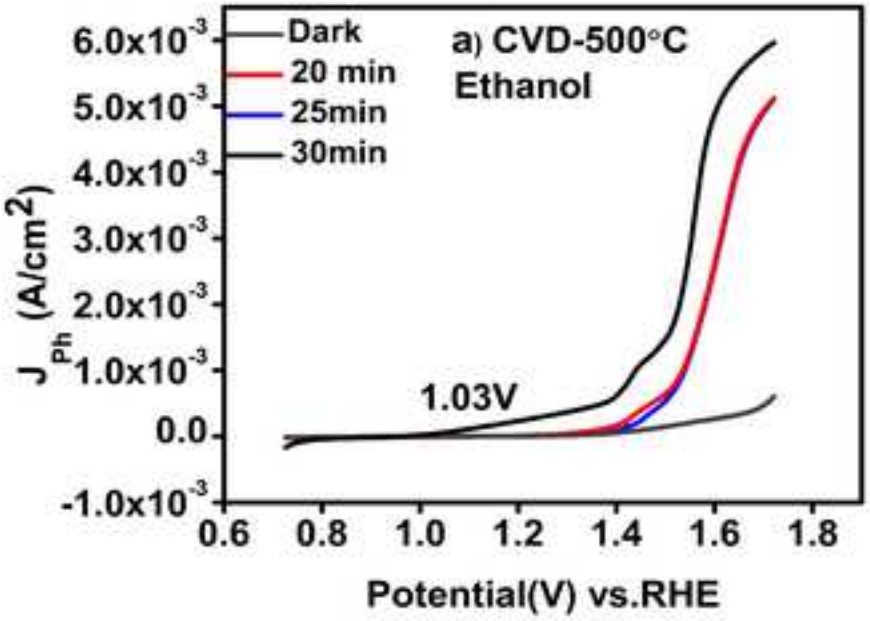

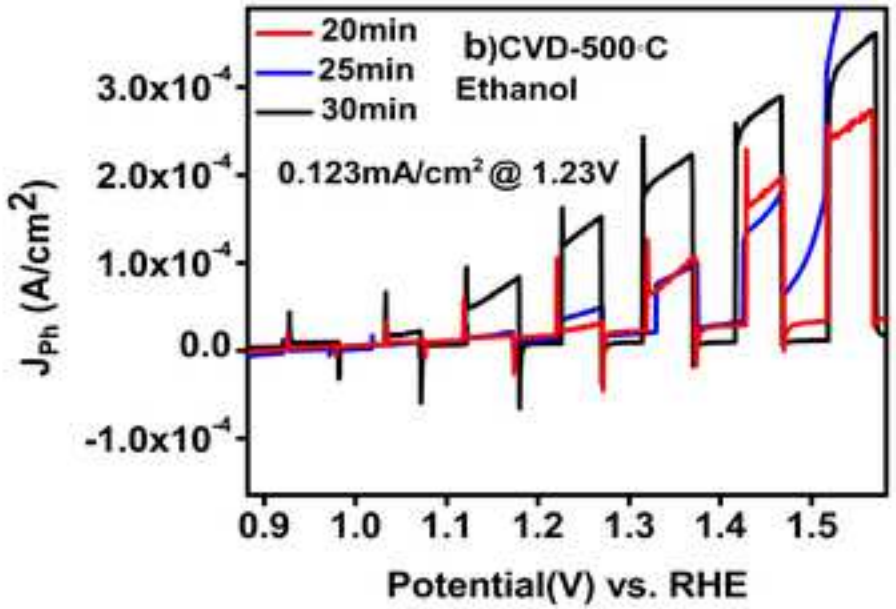

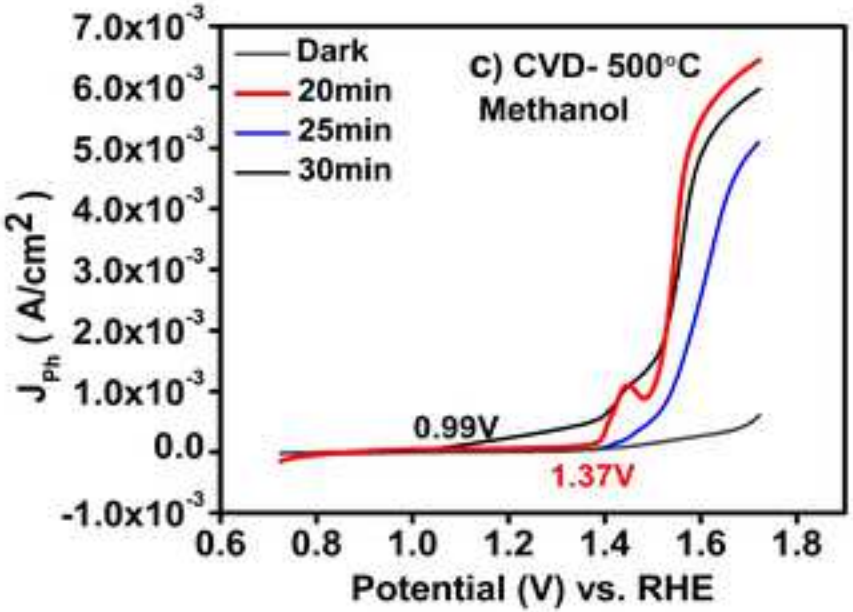

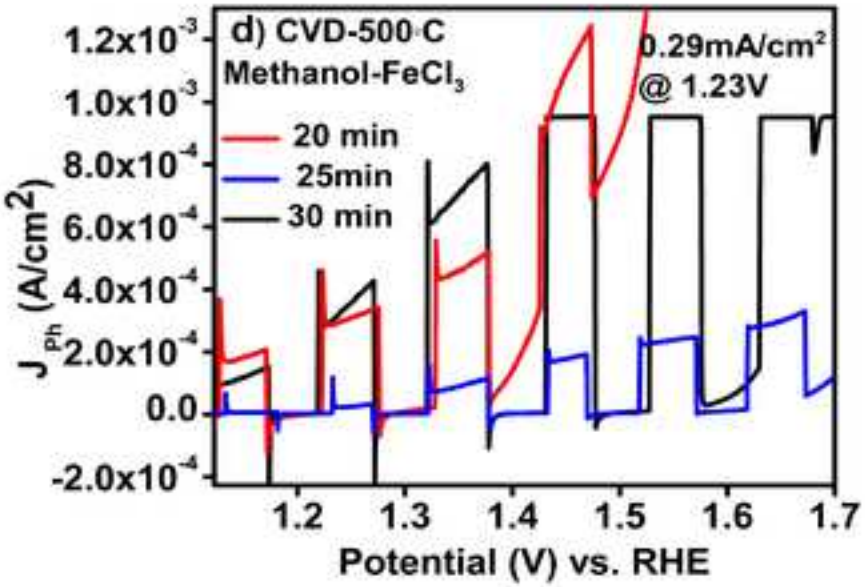

Figure 7

Click here to access/download;Figure;Fig.7.jpg

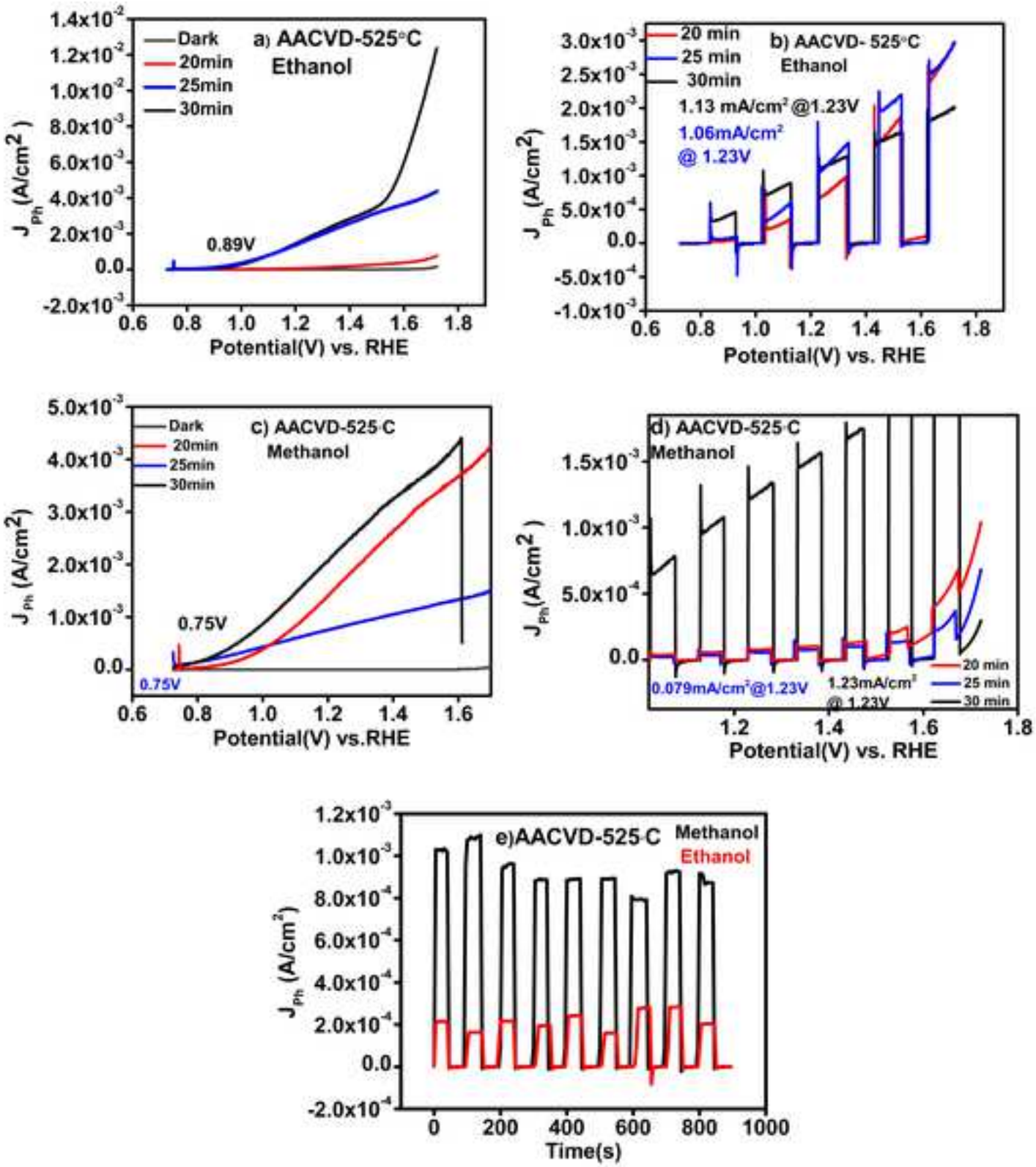

Figure 8

Click here to access/download;Figure;Fig.8.jpg